



LJMU Research Online

Andredaki, M, Vontas, K, Georgoulas, A, Miché, N and Marengo, M

The effect of channel aspect ratio on flow boiling characteristics within rectangular micro-passages

<http://researchonline.ljmu.ac.uk/id/eprint/17744/>

Article

Citation (please note it is advisable to refer to the publisher's version if you intend to cite from this work)

Andredaki, M, Vontas, K, Georgoulas, A, Miché, N and Marengo, M (2021) The effect of channel aspect ratio on flow boiling characteristics within rectangular micro-passages. International Journal of Heat and Mass Transfer. 183 (C). ISSN 0017-9310

LJMU has developed **LJMU Research Online** for users to access the research output of the University more effectively. Copyright © and Moral Rights for the papers on this site are retained by the individual authors and/or other copyright owners. Users may download and/or print one copy of any article(s) in LJMU Research Online to facilitate their private study or for non-commercial research. You may not engage in further distribution of the material or use it for any profit-making activities or any commercial gain.

The version presented here may differ from the published version or from the version of the record. Please see the repository URL above for details on accessing the published version and note that access may require a subscription.

For more information please contact researchonline@ljmu.ac.uk

<http://researchonline.ljmu.ac.uk/>

The effect of channel aspect ratio on flow boiling characteristics within rectangular micro-passages

Manolia Anredaki¹, Konstantinos Vontas¹, Anastasios Georgoulas¹, Nicolas Miché¹, Marco Marengo¹

¹Advanced Engineering Centre, School of Architecture Technology and Engineering, University of Brighton Lewes Road, BN2 4GJ, Brighton, East Sussex, U.K

Corresponding author: M.Andredaki@brighton.ac.uk

Abstract

In the present paper, a fundamental analysis on the effect of the channel aspect ratio on the bubble dynamics and heat transfer characteristics for the early transient stages of the bubble growth within confined microchannels of rectangular cross-section, under saturated flow boiling conditions, is conducted, utilising high resolution, 3D, transient, conjugate heat transfer simulations. The open-source toolbox OpenFOAM is applied for the simulations, utilising a custom, user-enhanced, diabatic Volume OF Fluid (VOF) solver. Two different series of numerical simulations are performed, focused on a single nucleation event from a single nucleation site and a single nucleation event from multiple, arbitrarily located, nucleation sites, respectively. In each series, three different values of channel aspect ratio are considered, corresponding to a narrow, a square, and a wide microchannel. For the first series, the simulations are performed for a low, a medium, and a high value of applied heat flux and mass flux. For the second series, only the lower values of applied heat flux and mass flux are used for each channel aspect ratio, since this constitutes the worst-case scenario from the overall heat transfer performance point of view, among the cases examined in the first series of simulations. The micro-passage aspect ratio has a significant effect in the generated bubble dynamics during the onset of the nucleate boiling regime, as the bubbles grow within the confined liquid crossflow. This alteration of the generated interfacial dynamics, in effect, regulates the size and position of the contact areas of the generated bubbles with the microchannel walls, with a direct effect in the individual contribution and therefore, the balance between the contact line and the liquid film evaporation mechanisms. Moreover, the work presents the quantification of the effect of the solid domain thermal inertia on the whole process and in particular on the local Nusselt numbers. It is evident that considering conjugate heat transfer in numerical simulations of flow boiling is compulsory in order to predict the physical processes in a correct form.

Keywords: flow boiling, microchannels, multiphase flow, VOF, conjugate heat transfer, aspect ratio

1. Introduction

Due to the continuous increase in the performance characteristics and miniaturisation trends of high-power density electronic components in applications such as computer chips, Insulated Gate Bipolar Transistors, Fuel Cells, their efficient thermal management has become a challenging issue. It has been reported that by 2026, the average heat flux that needs to be dissipated from computer chips is expected to reach values in the range of 2-4.5 MW/m² [1]. Similarly, Insulated Gate Bipolar Transistor (IGBT) modules, at the chip level, might reach heat flux values in the range of 6.5-50 MW/m². Conventional cooling methods, such as forced air cooling or pumped liquid cooling, cannot cope with such high heat dissipation demands. Flow boiling heat transfer within microchannel heat sinks has been already recognised as one of the most efficient thermal management solutions for such high-power density electronic components, being able to dissipate heat fluxes in the order of MW/m² [2]. Despite this fact, cooling of micro-electronics utilising flow boiling microchannel heat sinks is not yet commercially used and it is still limited to laboratory applications. This is mainly due to the lack of accurate design correlations as well as the lack of understanding of several underpinned principles and mechanisms. Karayiannis and Mahmoud [3] have already reported the still open fundamental research aspects and issues that are responsible for this lack. One of these open research aspects is the effect of channel geometry. In particular, in the case of rectangular micro-channels, the developed flow patterns, the heat transfer mechanisms and rates as well as the encountered pressure drops, can be affected by the aspect ratio of the channel cross-section, defined as the ratio of the channel width W over the channel height H ($\beta = W/H$).

One of the first studies that identified the critical geometric parameters that affect flow boiling heat transfer and flow patterns in microchannels was the work by Harirchian and Garimella [4]. They investigated experimentally seven different silicon test pieces containing parallel microchannels, with a perfluorinated dielectric fluid, Fluorinert FC-77, of widths ranging from 100 to 5850 μm , all with a depth of 400 μm . It was shown that for a fixed channel depth, the heat transfer coefficient was independent of channel width for microchannels of widths 400 μm and larger, with the flow regimes in these microchannels being similar; nucleate boiling was found to be dominant over a wide range of heat fluxes. They later expanded their investigation by five additional microchannel test pieces with channel depths of 100 and 250 μm and widths ranging from 100 to 1000 μm [5]. Flow visualisations were performed using a high-speed digital video camera to determine the flow regimes, with simultaneous local measurements of the heat transfer coefficient and pressure drop. The aim of this additional study was to investigate as independent parameters the channel width and depth as well as the aspect ratio and cross-sectional area on boiling heat transfer in microchannels, based on an expanded database of experimental results. The flow visualizations and heat transfer results shown that the microchannel width, depth, or aspect ratio individually do not determine boiling mechanisms

and heat transfer in micro-channels; instead, it is the cross-sectional area of the microchannels that plays a determining role. In microchannels with a cross-sectional area of 0.089 mm^2 and larger, nucleate boiling is dominant up to very high heat fluxes, resulting in an independence of heat transfer coefficient on channel dimensions. In these microchannels, as the aspect ratio β increases, flow patterns become asymmetric with respect to the channel width, i.e., two different flow patterns might be distributed side by side across the width of the channel.

Singh et al. [6] focused on the impact of varying the aspect ratio of rectangular microchannels, on the overall pressure drop involving water boiling. Rectangular microchannels were fabricated with varying aspect ratios (β) but constant hydraulic diameter of $142 \pm 2 \text{ }\mu\text{m}$ and length of 20 mm. The invariant nature of the hydraulic diameter is confirmed through two independent means: physical measurements using a profilometer and by measuring the pressure drop in a single-phase fluid flow. These experimental results show that the pressure drop for two-phase flow in rectangular microchannels experiences minima at an aspect ratio of about 1.6. The minimum is possibly due to opposing trends of frictional and acceleration pressure drops, with respect to aspect ratio. In a certain heat flux and mass flux range, it was observed that the two-phase pressure drop was lower than the corresponding single-phase value. This was also among the first studies to investigate the effect of aspect ratio in two-phase flow in microchannels.

In their study, Markal et al. [7] investigated experimentally the effect of aspect ratio on the saturated flow boiling characteristics of deionized water in parallel rectangular microchannels. Detailed flow visualizations were conducted as well as temperature and pressure measurements. Effects of heat and mass flux were examined too. Six different silicon microchannel heat sinks, each of which consists of 29 parallel rectangular microchannels, have been used. In order to determine the effect of the aspect ratio (β), the microchannels having different widths and heights but same hydraulic diameters ($100 \text{ }\mu\text{m}$) were used. Experiments were conducted for various values of the mass flux covering 151, 195, 238, 281 and $324 \text{ kg/m}^2\text{s}$, the values of the wall heat flux in the range of $71\text{--}131 \text{ kW/m}^2$ and various values of the aspect ratio including 0.37, 0.82, 1.22, 2.71, 3.54 and 5.00. The inlet temperature of deionized water was kept constant at $50 \pm 1 \text{ }^\circ\text{C}$ through the tests. It was found that the heat transfer coefficient increases with an increase in the aspect ratio up to a value of 3.54 and then decreases. The value of 1.22 has been appeared as a threshold value for the heat transfer coefficient. Additionally, there was no regular relationship identified between the aspect ratio and the resulted pressure drop. The flow visualization results provide key findings for underlying physical mechanisms. Quasi-periodical rewetting and drying phenomena, rapid bubble growth and elongation towards both upstream and downstream of the channels and reverse flow were observed in parallel microchannels and strong interactions were obtained between neighbouring channels.

In a more recent work by Markal et al. [8], using the experimental data from their previous work [7], a new correlation including the aspect ratio effect was proposed to predict the heat transfer coefficient for saturated flow boiling in microchannels. The proposed correlation showed very good predictions with an overall Mean Absolute Error (MAE) of 16.9% and 86.4%, 96.2% and 99.5% of the predicted data falling within ± 30 , ± 40 and $\pm 50\%$ error bands, respectively.

In the work by Wang et al. [9], flow boiling heat transfer in high aspect ratio (β) microchannels was experimentally investigated. Three high-aspect-ratio rectangular micro-channels were used, with the hydraulic diameters of which being 571 μm , 762 μm and 1454 μm . Mass fluxes of 11.2 $\text{kg m}^{-2} \text{s}^{-1}$, 22.4 $\text{kg m}^{-2} \text{s}^{-1}$ and 44.8 $\text{kg m}^{-2} \text{s}^{-1}$ and a wide range of heat fluxes were applied. Visualisation results, thermography measurements and heat transfer characteristics of FC-72 and ethanol were obtained. Moreover, ten existing correlations for macro-, mini- and micro-channels were assessed. For ethanol, good predictions of three micro-channel correlations were achieved (MAE = 16.4–18.8%). However, all the correlations showed very high MAE for FC-72 (MAE = 80.7–641.3%). It was found that liquid properties and the unique high-aspect-ratio micro-channel geometry are crucial in developing a more accurate correlation. A modified correlation was therefore proposed for FC-72 and ethanol with a MAE of 23.6%. They concluded that the effects of channel aspect ratio and liquid properties need to be emphasised to develop more accurate correlations for flow boiling heat transfer in high-aspect-ratio micro-channels.

The investigation by Soupremanien et al. [10] presented experiments conducted with two single rectangular mini-channels of same hydraulic diameter (1.4 mm) and different aspect ratios ($1/\beta = H/W$) for conditions of horizontal boiling flow. The Forane® 365 HX used was subcooled ($\Delta T_{\text{sub}} = 15 \text{ }^\circ\text{C}$) for all the boiling curves presented in their work. Local heat transfer coefficients were measured for heat flux ranging from 25 to 62 kW m^{-2} and mass flux from 200 $\text{kg m}^{-2} \text{s}^{-1}$ to 400 $\text{kg m}^{-2} \text{s}^{-1}$. The boiling flows were observed with two different cameras (depending on the flow velocity) through a visualization window. The flow patterns in the two channels were compared for similar conditions. The results show that the boiling heat transfer coefficient and the pressure drop values are different for the two single mini-channels. For low heat flux condition, the channel with lowest aspect ratio ($H/W = 0.143$) had a higher heat transfer coefficient. On the other hand, for high heat flux condition, the opposite situation occurred, namely the heat transfer coefficient became higher for the channel with highest aspect ratio ($H/W = 0.43$). This is probably due to the earlier onset of dryout in the channel with lowest aspect ratio. For the two cases of heating, the pressure drop for the two-phase flow remained lower for the channel with the lowest aspect ratio. These results show that the aspect ratio plays a substantial role for boiling flows in rectangular channels. As for single-phase flows, the heat transfer characteristics are significantly influenced (even though the hydraulic diameter remains the same) by this parameter.

Lee and Garimella [11] performed numerical simulations, based on the finite volume method, to predict steady, laminar heat transfer coefficients in hydrodynamically developed but thermally developing flow within rectangular microchannels of different aspect ratios ($1/\beta = H/W$). Generalised correlations for both the local and average Nusselt numbers in the thermal entrance region were proposed. The proposed correlations allow accurate predictions of the thermal performance of microchannel heat sinks.

Two years later, Lee and Garimella [12] investigated experimentally flow boiling in arrays of parallel microchannels, using a silicon test piece with embedded discrete heat sources and integrated local temperature sensors. The considered microchannels ranged in width from 102 μm to 997 μm , with the channel depth being nominally 400 μm in each case resulting in different aspect ratios ($1/\beta = H/W$). Each test piece had a footprint of 1.27 cm by 1.27 cm with parallel microchannels diced into one surface. Twenty-five microsensors integrated into the microchannel heat sinks allowed for accurate local temperature measurements over the entire test piece. The experiments were conducted with deionized water which enters the channels in a purely liquid state. Results were presented in terms of temperatures and pressure drops as a function of imposed heat flux. The experimental results allowed a critical assessment of the applicability of existing models and correlations in predicting the heat transfer rates and pressure drops in microchannel arrays and led to the development of models for predicting the two-phase pressure drop and saturated boiling heat transfer coefficient.

Wang and Sefiane [13] investigated experimentally flow boiling heat transfer in high aspect ratio micro-channels with FC-72. Three channels with different hydraulic diameters (571, 762 and 1454 μm) and aspect ratios ($\beta = 20, 20$ and 10) were selected. The tested mass fluxes were 11.2, 22.4 and 44.8 $\text{kg m}^{-2} \text{s}^{-1}$ and heat fluxes ranging from 0–18.6 kW m^{-2} . In their study, average heat transfer coefficient and local heat transfer coefficient along stream-wise direction were measured as a function of heat flux and vapour quality respectively. Slug-annular flow and annular flow were the main flow regimes, while convective boiling is found to be the dominant heat transfer mechanism. Among other conclusions, they argued that the unique geometry of the high aspect ratio flat micro-channel is crucial in determining the flow regimes and heat transfer mechanism.

Fu et al. [14] investigated experimentally the effect of aspect ratio ($1/\beta = H/W$) of copper-based microchannel heat sinks with approximately the same hydraulic diameter (about 1.12 mm) on flow boiling heat transfer and critical heat flux (CHF), using liquid HFE-7100 as working fluid. They performed experiments with mean aspect ratios of 0.83, 0.99, 1.65, 2.47, 4.23, and 6.06. The results demonstrated that the aspect ratio of microchannels affected the boiling heat transfer significantly. The wall heat flux at a given wall superheat and wall critical heat flux demonstrate the peak value at

the aspect ratio of 0.99 possibly due to copious existence of the liquid film around the corner. The experimental results for the critical heat flux were further compared with existing correlations of flow boiling in a microchannel, and a new empirical correlation, incorporating the aspect ratio, was proposed. They concluded that the diverging design of the microchannel with a large aspect ratio and high mass flux is recommended to develop an electronic cooling system for the need of very high heat dissipation rates.

Candan et al. [15] investigated experimentally saturated flow boiling characteristics of deionized water in single rectangular minichannels of hydraulic diameter 1.2 mm, 48 mm length and aspect ratio ($\beta = W/H$) range 0.25–4. Experiments have been conducted for various values of the mass flux and the wall heat flux. Flow visualisation has been used as a complementary technique for a deeper physical understanding of flow phenomena. The results shown that the channel aspect ratio has a significant effect on both the local two-phase heat transfer coefficient and the total pressure drop. They reported that the best performance was achieved with $\beta = 1$ due to the presence of uniform liquid film at the sharp corners of square channels while the poorest performance occurred with $\beta = 0.25$ due to early local dry-out. The heat transfer coefficient near the channel exit was found to increase with heat flux, mass flux and vapor quality and they concluded that the dominant heat transfer mechanism is nucleate boiling, with dominant flow patterns bubbly/slug flow.

Al- Zaidi et al [16] studied the effect of aspect ratio ($\beta = W/H$) on the flow boiling heat transfer of HFE-7100 in horizontal multi-microchannels, with aspect ratios of 0.5, 1 and 2 and the same hydraulic diameter, base area and average surface roughness. They concluded that, the channel aspect ratio had a significant effect on the heat transfer results in the studied range. The bubble size in the larger aspect ratio was smaller than that in the smaller aspect ratio. The slug length became longer in the smaller aspect ratio. Additionally, the heat transfer coefficient increased with heat flux, while there was insignificant effect of mass flux. Moreover, the local heat transfer coefficient was found to increase with aspect ratio. Finally, they also highlighted the importance different flow and thermal behaviour of the channels with different aspect ratios to be further investigated.

Lee and Mudawar [17], [18] examined experimentally the effects of micro-channel hydraulic diameter and aspect ratio ($1/\beta = H/W$) on flow boiling heat transfer of HFE-7100 in four horizontal rectangular multi-microchannels made of oxygen-free copper, with hydraulic diameter ranging from 0.176 to 0.416 mm and aspect ratio (width to height) range of 0.25–0.41. They reported that the heat sink with smaller hydraulic diameter exhibited better heat transfer performance compared to channels with large diameters. This was attributed to an increase in the wetted area and mass velocity for the small hydraulic diameter. Reviewing the work by Lee and Mudawar [17], [18], Özdemir et al. [19] reported that the effect of diameter was studied while the channel aspect ratio was not fixed. Hence,

the change in the wetted area could be due to a change in the aspect ratio rather than a change in diameter.

In their recent work, Özdemir et al. [19] presented the experimental results of flow boiling of water in single rectangular microchannels. Three rectangular copper microchannels having the same hydraulic diameter (0.56 mm) and length (62 mm) but different aspect ratios ($\beta = 0.5, 2.56, \text{ and } 4.94$) were investigated using de-ionized water as the working fluid. The experiments were conducted over the experimental range of mass flux 200–800 kg/(m²s), heat flux 4–1350 kW/m² and inlet subcooling of ~14 K. The results showed that the channel with smaller aspect ratio exhibited better heat transfer performance up to certain heat fluxes (~480–500 kW/m²), whilst the effect of channel aspect ratio became insignificant for higher heat fluxes. The flow boiling patterns were observed and the main flow regimes were bubbly, slug, churn, and annular flow. Flow reversal was also observed that caused a periodic flow in the two microchannels having smaller aspect ratio. A comparison of the experimental results with widely used macro and micro-scale heat transfer correlations is presented. The macro-scale correlations failed to predict the experimental data while some micro-scale correlations could predict the data reasonably well. Özdemir et al. [19] reported, reviewing previous investigations, that the effect of aspect ratio is very complex. Markal et al. [7] concluded that the heat transfer coefficient increased with increasing heat flux in deep channels while it decreases with heat flux in shallow channels. On the contrary, Candan et al. [15] reported that the deep channels exhibited poor heat transfer performance due to the occurrence of dry-out, while Al-Zaidi et al. [16] reported that, for HFE-7100, the local heat transfer coefficient increases with increasing aspect ratio for all their tested conditions.

In their work, Wang et al. [20] investigated numerically the influence of geometric parameters on the flow and heat transfer characteristics of rectangular, trapezoidal and triangular shaped microchannel heat sinks. They found that the microchannel with high aspect ratio ($1/\beta = H/W$), long wetted perimeter and small hydraulic diameters usually have low thermal resistance and high pressure drop and, for rectangular microchannels, the best performance is achieved with aspect ratio among 8.904–11.442. It is important to mention here that the proposed investigation considers conjugate heat transfer, however, between solid and single-phase flow domains, as it does not constitute a boiling heat transfer investigation.

In a more recent work [21], a numerical study, utilised ANSYS CFX 14.5, commercially available CFD code, has been carried out to investigate the heat transfer enhancement and fluid flow characteristics for various aspect ratios ($1/\beta = H/W$) of single-phase rectangular micro channel heat sinks (MCHS). The channel size optimization has been carried out numerically to obtain the effective heat removal from the MCHS. Average convective heat transfer coefficient, outlet temperature,

friction and pressure drop, pumping power and thermal resistance have been plotted against Reynolds number. The Nusselt number has been plotted as a function of Reynolds number for three heat sinks with different aspect ratios: 20, 30 and 46.66. From the numerical analysis, aspect ratio of 30 is the preferred choice and amount of the heat removal is at an optimum level. The proposed investigation also considers conjugate heat transfer, between solid and single-phase flow domains.

More recently Magnini and Matar [22] performed a systematic numerical analysis examining the effect of the channel shape on the bubble dynamics and heat transfer, under flow boiling conditions within microchannels, using their customised VOF method in OpenFOAM in order to capture the liquid-vapour interface dynamics. A benchmark flow model was utilised, where a single isolated Taylor bubble was seeded at the channel upstream and transported by a liquid flow across a diabatic section, which was heated by a constant and uniform heat flux. Flow conditions that apply well to the flow boiling of water or refrigerant fluids in sub-millimetre channels at low heat flux ($\sim 10\text{kW/m}^2$) were investigated, with cross-section aspect ratios ($\beta = W/H$) ranging from 1 to 8, while the hydraulic diameter of the channel was fixed. It was shown that the heat transfer performances for different channel shapes are closely related to the perimetral distribution of the liquid film surrounding the elongated vapour slugs that are generated due to liquid film evaporation. It was also illustrated that square channels ($\beta = 1$) exhibit the highest heat transfer coefficients at low flow rates, due to a very thin liquid film that forms at the centre of the wall, however, they are more at a risk of film dryout. High aspect ratio rectangular channels may be beneficial at larger flow rates, as they promote the formation of an extended liquid film that covers up to 80% of the cross-section perimeter. Finally, at larger aspect-ratios, the average heat transfer coefficient along the shorter wall becomes orders of magnitude smaller than the value detected along the longer wall, owing to a strong asymmetry in the liquid film perimetral distribution. The proposed work constitutes a two-phase flow investigation related to flow boiling within microchannels, however, it does not account for conjugate heat transfer between solid and two-phase flow domains.

From all these previous investigations it is evident that there is a significant effect of the channel aspect ratio on the heat transfer coefficient. However, the proposed effect is not clearly quantified and explained in most cases and needs further investigation. Furthermore, most of the previous investigations examine the effect of the aspect ratio on established quasi-steady state two-phase flow conditions and no attempt has been made so far to examine, identify, and quantify the effect of aspect ratio in the first transient stages of the two-phase flow development from bubble nucleation up to two-phase flow development. Therefore, the main objective of the present paper is to extend the current state of the art and perform a fundamental analysis of the role of the channel aspect ratio focusing both at the bubble dynamics and heat transfer characteristics at the early transient stages of the bubble growth within confined micro-passages, under saturated flow boiling conditions.

According to the Authors' best knowledge this is conducted for the first time and constitutes the main novelty of the present paper. For this purpose, high-resolution, 3D, interface resolving numerical simulations are conducted with a custom, enhanced, diabatic version of the VOF method in OpenFOAM. It is also important to highlight here that for the first time conjugate heat transfer simulations between solid and two-phase fluid domains that account for accurate dynamic contact angle modelling are utilised to study the early transient stages of the bubble growth dynamics, focusing on the effect of channel aspect ratio.

The proposed modelling enhancements involve an appropriate treatment for spurious velocities dampening (which is really important for small scale flows), an improved dynamic contact angle treatment to accurately account for wettability effects, and the implementation of a phase-change model in the fluid domain that also accounts for Conjugate Heat Transfer (CHT) with solid domains [23]–[28].

Ethanol is selected as the working fluid and stainless steel as the solid material for the heated wall for all of the considered microchannels. Three different aspect ratios are considered ($\beta = 0.5, 1.0, 2.5$), and for all three different aspect ratios, a fixed channel hydraulic diameter of $D_H = 200 \mu\text{m}$ was used. Three different values of applied heat flux ($q'' = 20, 50, 100 \text{ kW/m}^2$) and mass flux ($\dot{m} = 73.7, 149.6, 249.7 \text{ kg/m}^2\text{s}$ for $\beta = 0.5$, $\dot{m} = 98.2, 199.5, 392.9 \text{ kg/m}^2\text{s}$ for $\beta = 1.0$ and $\dot{m} = 171.7, 349.1, 687.6 \text{ kg/m}^2\text{s}$ for $\beta = 2.5$) are also considered. Since the hydraulic diameter of the channels with the different aspect ratios as well as the applied heat fluxes in each sub-series of runs remain constant, while both the height and the width of the channels vary to achieve the different aspect ratios, the total power dissipated in each case is different. Therefore, the low, medium and high mass fluxes, applied for each channel aspect ratio, were varied accordingly in order to maintain the same total power to mass flux ratios, i.e., maintaining a constant enthalpy variation.

Two different series of simulations are performed. In the first series, a single bubble nucleus/seed is placed upstream, close to the inlet on the conjugate heat transfer boundary between the solid and fluid domains, that then evaporates and grows in a previously developed initial hydrodynamic and thermal boundary layer. The first 10 ms from the bubble nucleation event are considered in each case. In the second series of simulations, a more realistic initial scenario is considered for each channel aspect ratio, where 30 arbitrary distributed bubble seeds are placed simultaneously on the conjugate boundary. It is shown that the variation of the aspect ratio of a microchannel has a significant effect in the local heat transfer coefficient, due to an enhancement of the single-phase heat transfer, in combination with the alteration of the underpinned bubble growth dynamics, which result in different contributions of contact line versus liquid film evaporation.

2. Numerical Method

2.1. Governing Equations

As mentioned previously, the numerical simulations of the present paper are conducted with the open-source toolbox OpenFOAM, utilising a customised enhanced VOF solver. The proposed solver enhancements involve a treatment for spurious velocities dampening (a well-known defect of VOF methods), an improved dynamic contact angle treatment to accurately account for wettability effects as well as the implementation of a phase-change model in the fluid domain, accounting for CHT with a solid domain. In this section, the governing equations for mass, momentum, energy, and volume fraction are presented. The liquid and vapour phases are both treated as incompressible, Newtonian fluids. The proposed solver has been extensively validated and applied in the past by the authors' research team against various cases of adiabatic and diabatic bubble and droplet dynamics. Further details can be found in [23]–[29].

The mass conservation equation is given as:

$$\nabla \cdot (\rho \vec{U}) = \dot{\rho} \quad (1)$$

where \vec{U} is the fluid velocity and ρ is the bulk density. The source term on the right-hand side $\dot{\rho}$ accounts for the phase change. The conservation of momentum is given by the following equation:

$$\frac{\partial}{\partial t}(\rho \vec{U}) + \nabla \cdot (\rho \vec{U} \vec{U}) - \nabla \cdot \left\{ \mu \left[\nabla \vec{U} + (\nabla \vec{U})^T \right] \right\} = -\nabla p + \vec{f}_{ST} + \vec{f}_g \quad (2)$$

where p is the pressure and μ is the bulk dynamic viscosity. The momentum source terms on the right-hand side of the equation account for the effects of surface tension (\vec{f}_{ST}) and gravity (\vec{f}_g), respectively. The surface tension term is modelled according to the classical approach of Brackbill et al. [30]. The conservation of energy balance in the fluid domain is given by the following equation:

$$\frac{\partial}{\partial t}(\rho c_p T) + \nabla \cdot (\vec{U} \rho c_p T) - \nabla \cdot (\lambda \nabla T) = \dot{h} \quad (3)$$

where c_p is the bulk heat capacity, T the temperature field, and λ is the bulk thermal conductivity. The source term on the right-hand side of the equation (\dot{h}) represents the contribution of the enthalpy of evaporation/condensation or else the cooling/heating associated with the latent heat of the phase-change. The volume fraction α is advected by the flow field by the following equation:

$$\frac{\partial \alpha}{\partial t} + \nabla \cdot (\alpha \vec{U}) - \nabla \cdot (\alpha(1 - \alpha) \vec{U}_r) = \frac{\dot{\rho}}{\rho} \alpha \quad (4)$$

Interface sharpening is very important in simulating two-phase flows of two immiscible fluids. In OpenFOAM, the sharpening of the interface is achieved artificially by introducing the extra compression term $\nabla \cdot (\alpha(1 - \alpha)\vec{U}_r)$ in Equation (4). \vec{U}_r is an artificial compression velocity. The source term on the right-hand side of the Equation (4) $(\frac{\dot{\rho}}{\rho}\alpha)$ is needed because, due to the local mass source terms, the velocity field is not free of divergence. Finally, the bulk fluid properties are computed as the averages over the liquid and vapour phases, weighted with the volume fraction α , i.e. $\rho = \alpha\rho_l + (1 - \alpha)\rho_v$.

As also mentioned previously, the VOF-based solver that is used in the present investigation has been modified accordingly to account for an adequate level of spurious currents suppression, a well-known defect of VOF methods in general. More details on the proposed implementation and validation can be found in the paper by Georgoulas et al [23].

The conservation of energy equation in the solid domains is defined as:

$$\frac{\partial}{\partial t}(\rho_s c_{ps} T) = \nabla \cdot (\lambda_s \nabla T) \tag{5}$$

where ρ_s and c_{ps} are the solid density and heat capacity respectively. The coupling at the interface between the solid and fluid region is achieved iteratively through the following conditions:

$$T_f = T_s, \quad \lambda_f \frac{\partial T_f}{\partial n} = \lambda_s \frac{\partial T_s}{\partial n} \tag{6}$$

where T_f is the temperature at the fluid side and T_s is the temperature at the solid side of the conjugate heat transfer boundary, λ_f is the thermal conductivity of the fluid domain and λ_s is the thermal conductivity of the solid domain.

2.2. Phase Change Model

The phase change model originally proposed by Hardt and Wondra [31] has been also implemented in the improved OpenFOAM VOF solver that is used in the present investigation. According to the proposed approach, the mass flux at the interface of the two phases (j_{evap}), which is created from either evaporation or condensation, is calculated with the following equation:

$$j_{evap} = \frac{T_{int} - T_{sat}}{R_{int} h_{lv}} \tag{7}$$

where T_{int} is the temperature of the interface, T_{sat} is the saturation temperature, R_{int} is the interfacial heat resistance and h_{lv} is the latent heat of evaporation or condensation at the saturation temperature.

The amount of liquid that evaporates or the amount of vapour that condenses is calculated locally and the resulting source term field is smeared over a few cells in order to avoid numerical instabilities.

The interfacial heat resistance is calculated by:

$$R_{\text{int}} = \frac{2 - \gamma}{\gamma} \frac{\sqrt{2\pi R_{\text{gas}} T_{\text{sat}}^{3/2}}}{h_{\text{lv}}^2 \rho_{\text{v}}} \quad (8)$$

Eq. (8) represents a fitting function. This is proved by the varying uncertainty of the γ parameter, contained within the range $0 < \gamma < 1$. For all cases presented in the present paper, the parameter γ , which can be referred to as the evaporation/condensation coefficient is taken to be equal to 1. The term R_{gas} represents the specific gas constant of the fluid which is calculated as R/M , where R is the universal gas constant and M is the molar mass of the working fluid.

The mass flux from evaporation and condensation, calculated through Eq. (7) is added to the conservation equations, through the definition of an appropriate volumetric source term. The volumetric source term is calculated by multiplying the flux of evaporated/condensed mass at the interface by the magnitude of the volume fraction gradient. This definition is explicit in the equation below:

$$\dot{\rho}_0 = j_{\text{evap}} |\nabla \alpha| \quad (9)$$

To calculate the “Net Mass Flow” one should then integrate this initial source term field through the entire interface. To do this the following equation was used:

$$\dot{m}_{\text{int}} = \iiint \dot{\rho}_0 \, dV \quad (10)$$

The “Net Mass Flow” is very relevant to guarantee mass conservation in the domain. The mass source magnitudes of liquid and vapour should be equal, as they represent the net evaporation rate. In order to avoid computational instabilities, the initially calculated sharp source term is smeared over a finite number of computational cells. This is done through the solution of a diffusion equation for the smooth distribution of source terms. This is shown below:

$$\dot{\rho}_1 - \nabla \cdot [(D\Delta\tau)\nabla\dot{\rho}_1] = \dot{\rho}_0 \quad (11)$$

As it can be seen, an artificial time step $\Delta\tau$ is utilised for this purpose, and Neumann boundary conditions are applied in all boundaries of the domain, for the smeared source term $\dot{\rho}_1$. Despite this artificial smearing of the original source term, the integral values of the sharp and the smooth fields remain the same. It is important to note that the overall width of the smeared field is proportional to the square root of diffusion constant “ D ” times the artificial time step “ $\Delta\tau$ ”. The chosen value of “ D ”

must be, in each case, adjusted to the mesh resolution to ensure smearing over a finite number of cells.

The next step in this process of avoiding computational instabilities, is to take the source terms in all cells that do not contain pure liquid or vapour ($\alpha < 1 - \alpha_{\text{cut}}$ and $\alpha > \alpha_{\text{cut}}$, where α_{cut} is set to 0.001) and artificially set them to zero. After this step, the interface cells are not subjected any more to source terms. Therefore, the interface is only transported by the calculated velocity field. This ensures that the transport algorithm for the volume fraction field and the associated interface compression (described previously) can work efficiently without any interference with the evaporation/condensation source term field. In order, however, to maintain continuity, the remaining source term field needs to be scaled accordingly on the liquid and the vapour side using appropriate scaling coefficients. This final scaling step ensures that the mass is globally conserved. The proposed scaling coefficients N_l (liquid phase) and N_v (vapour phase) are in effect the ratio of net mass flow \dot{m}_{int} (Equation 10), to the volume integrals (over the entire computational domain) of the smooth source term field, in each of the pure phases:

$$N_l = \dot{m}_{\text{int}} \left[\iiint (a - 1 + a_{\text{cut}}) \dot{\rho}_1 dV \right]^{-1} \quad (12)$$

$$N_v = \dot{m}_{\text{int}} \left[\iiint (a_{\text{cut}} - a) \dot{\rho}_1 dV \right]^{-1} \quad (13)$$

After this necessary scaling, the final source term field is calculated, using the following equation:

$$\dot{\rho} = N_v (\alpha_{\text{cut}} - \alpha) \dot{\rho}_1 - N_l (\alpha - 1 + \alpha_{\text{cut}}) \dot{\rho}_1. \quad (14)$$

This particular implementation has been extensively validated by the present Authors' research group in the past against existing analytical solutions of vapour bubbles growing in superheated liquid domains as well as against literature available experiments bubbles growing and detaching from superheated plates [32].

2.3. Dynamic Contact Angle Treatment

The utilised VOF-based solver includes also an implementation of the dynamic contact angle (DCA) model originally suggested by Kistler [33]. This implementation has been validated in the past against experiments available in the literature for droplet impact on flat surfaces with different wettability [29] as well as against experiments of pool boiling in biphilic surfaces [34], with excellent degree of convergence between the experimental measurements and the numerical predictions. Furthermore, it has been recently applied for the investigation of the effect of wettability in flow boiling characteristics within microchannels by the same Authors' team as the present paper [28].

In more detail, with this DCA treatment, the dynamic contact angle θ_d is given as a function of the contact line velocity (u_{cline}), through the capillary number Ca and the inverse of Hoffman's function. The θ_d , can be calculated by the following equation:

$$\theta_d = f_H [Ca + f_H^{-1} (\theta_{\text{eq}})] \quad (15)$$

where f_H^{-1} is the inverse function of the Hoffman's empirical function, which is given by:

$$f_H = \arccos \left\{ 1 - 2 \tanh \left[5.16 \left(\frac{x}{1 + 1.31x^{0.99}} \right) \right]^{0.706} \right\} \quad (16)$$

where x is equal to:

$$x = f_H [Ca + f_H^{-1} (\theta_{\text{eq}})] \quad (17)$$

The capillary number is defined as:

$$Ca = \frac{\mu u_{\text{cline}}}{\sigma} \quad (18)$$

The equilibrium angle θ_{eq} is replaced by either a limiting advancing or receding contact angle θ_a or θ_r , depending on the sign of the velocity vector at the contact line.

3. Application of Numerical Model

3.1. Computational Geometry, Mesh and Boundary Conditions

In Figure 1, the generated computational geometry, mesh and the applied boundary conditions are illustrated indicatively for $\beta = 0.5$. As it can be seen the computational mesh has been generated by discretising the computational domain in two parts; the solid domain and the fluid domain. A uniform, structured computational mesh, consisting of hexahedral elements is utilised. After a mesh independence study, an element size of $2\mu\text{m}$ was selected. The mesh independency study has been conducted in a recent, previous work [28], and it will be not further described here. The total number of cells for the solid domain is 4.05M and for the fluid domain is 13.5M.

The fluid domain dimensions (length, height, and width) are $L_f = 2.4$ mm, $H_f = 0.30$ mm, $W_f = 0.15$ mm, and the solid domain dimensions are $L_s = 2.4$ mm, $H_s = 0.09$ mm, $W_s = 0.15$ mm. For the geometry with $\beta = 1.0$ the fluid and solid domain dimensions are $L_f = 2.4$ mm, $H_f = 0.20$ mm, $W_f = 0.20$ mm and $L_s = 2.4$ mm, $H_s = 0.09$ mm, $W_s = 0.2$ mm, while the resulting total number of cells for the solid and fluid domain is 5.40M and 12.00M, respectively. Finally, for the geometry with $\beta = 2.5$ the fluid and solid domain dimensions are $L_f = 2.4$ mm, $H_f = 0.14$ mm, $W_f = 0.35$ mm and $L_s = 2.4$ mm, $H_s = 0.09$, $W_s = 0.35$ mm, while the total number of cells for the solid and fluid domain is 9.45M and 14.70M, respectively.

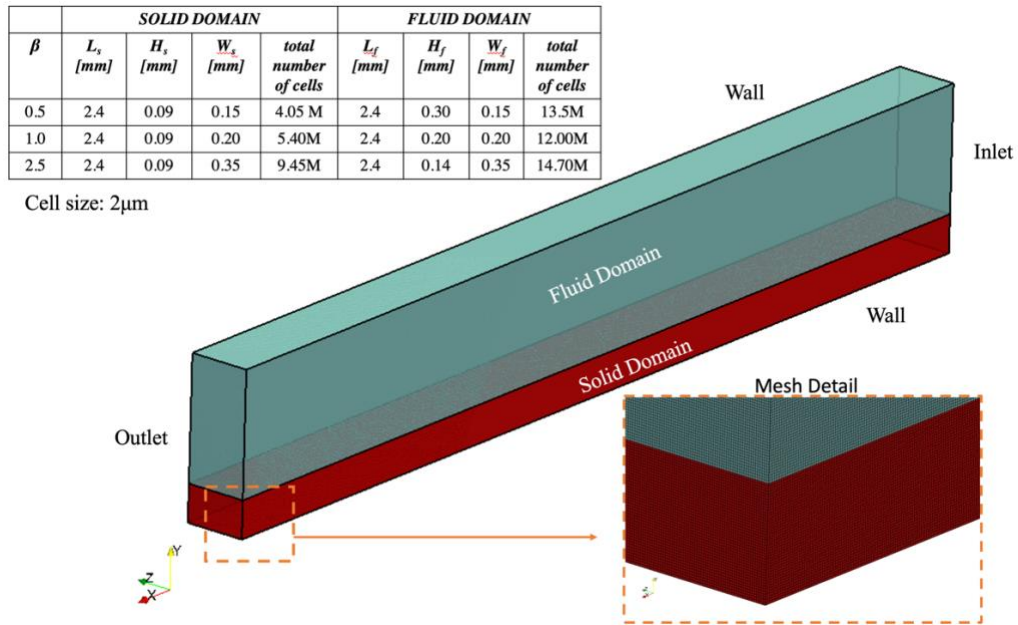


Figure 1. Computational domain, boundary conditions and mesh details (illustrated indicatively for $\beta = 0.5$).

For all cases considered, except from the inlet and outlet in the fluid domain and the bottom side of the solid domain, where a constant heat flux is applied, all the rest surfaces are considered to be adiabatic walls. At the walls, a standard no-slip velocity boundary condition was used with a fixed flux pressure boundary condition for the pressure values. Moreover, a dynamic contact angle boundary condition is imposed for the volume fraction field, by assigning the maximum advancing and minimum receding contact angle values from sessile drop measurements. For the sidewalls of the fluid and solid domains, as well as for the top wall of the fluid domain a zero gradient boundary condition was used for the temperature field. At the outlet, a fixed-value pressure boundary condition and a zero-gradient boundary condition for the volume fraction were used, while for the velocity values a special (combined) type of boundary condition was used that applies a zero-gradient, when the fluid mixture exits the computational domain and a fixed value condition to the tangential velocity component, in cases that the fluid mixture enters the domain. Finally, a zero gradient boundary condition for the temperature field was also prescribed at the outlet boundary. For the inlet, a constant uniform velocity value was imposed as well as a fixed flux pressure condition. The volume fraction value was assigned as unity, as saturated liquid only enters from the inlet during the calculations. Hence, the temperature of the liquid at the inlet was also fixed at the saturation temperature. As mentioned earlier, both the temperature values as well as the heat fluxes are coupled at the conjugate heat transfer interface, for each calculation time step, through an inner iteration process.

3.2. Numerical Simulation Set-up and Process

All simulations are performed in two main stages. During the first stage, a specified heat flux is applied to the bottom surface of the solid domain, and a single-phase liquid flow is considered

initially with saturated liquid flowing with a specified mass flow rate. This is run up to a point that a steady state condition is reached and both the initial hydrodynamic and thermal boundary layers have been developed. The velocity of the liquid U_1 is constant and uniform through the inlet boundary and the flow is laminar.

At the second stage, for the first series of numerical simulations, a small vapour nucleus (bubble seed) represented as a half-sphere with a radius of $20\ \mu\text{m}$ is artificially patched on the conjugate heat transfer boundary (interface between the fluid and solid domains) at $200\ \mu\text{m}$ from the channel inlet, at saturation temperature (Figure 2a). For the second stage of the second series of simulations, 30 arbitrary distributed bubble seeds are placed simultaneously on the conjugate heat transfer boundary (Figure 2b).

Since these initial bubble seeds, in both series of numerical simulations, are patched within the previously developed thermal boundary layer, where the temperature is higher than the saturation temperature, boiling occurs at the meniscus (solid/liquid/vapour triple line) as well as at the parts of the liquid/vapour interface away from the heated wall that are in contact with temperatures higher than the saturation temperature, due to the existing initial thermal boundary layer. It is important to mention that the present numerical model does not include any prediction of the onset temperature. Therefore, the nuclei bubble seeds are artificially imposed by user. This is a quite common approach that is followed in numerical investigations of flow boiling phenomena [35], [36]. However, this does not negatively impact the present investigation, as it focuses on the first transient stage of bubble development just after the appearance of the bubble seed on the heated wall.

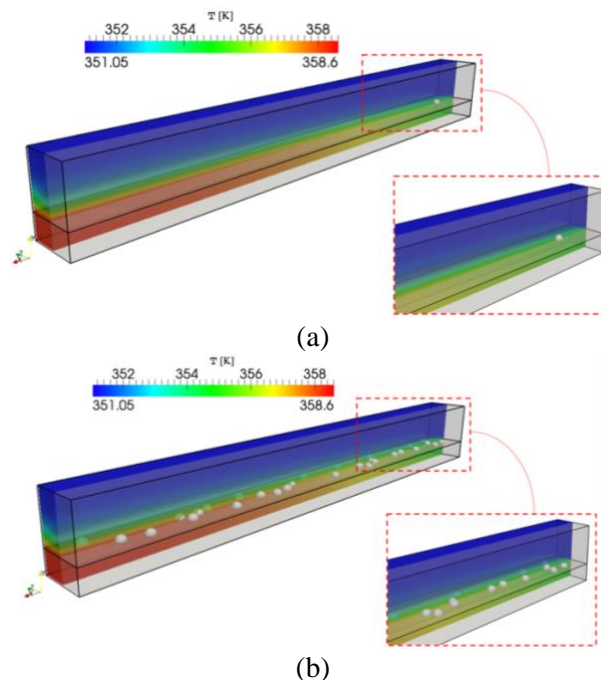


Figure 2. Initial condition for the second (two-phase) stage of numerical simulations for Series 1 (a) and Series 2 (b) numerical simulations. In both cases the initial condition that is illustrated indicatively here, corresponds to a channel aspect ratio of $\beta=1.0$, an applied heat flux of $q'' = 20\text{kW/m}^2$ and a mass flux of $G = 98.2\ \text{kg/m}^2\text{s}$.

It should be mentioned that for all of the simulations conducted for the present investigation the liquid and vapour phase properties are taken as these of ethanol liquid and vapour at the saturation equilibrium point for a pressure of $P_{sat} = 1$ bar, which corresponds to a saturation temperature of $T_{sat} = 351.05$ K (REFPROP NIST software [37]). Hence, the liquid and vapour densities were taken as $\rho_l = 736.78$ kg/m³ and $\rho_v = 1.63$ kg/m³, the liquid and vapour kinematic viscosities as $\nu_l = 6.01 \times 10^{-7}$ m²/s and $\nu_v = 6.37 \times 10^{-6}$ m²/s, the liquid and vapour thermal conductivities as $\lambda_l = 0.15$ W/mK and $\lambda_v = 0.02$ W/mK and the liquid and vapour heat capacities as $c_{p,l} = 3182$ J/kgK and $c_{p,v} = 1804$ J/kgK. For the solid domain, stainless steel properties are used. In more detail, the density of the solid domain is taken as $\rho = 7840$ kg/m³, the specific heat as $c_{p,s} = 500$ J/kgK and the thermal conductivity as $\lambda_s = 16.2$ W/mK. The surface tension coefficient was taken as $\sigma = 0.015$ N/m and the latent heat of evaporation as $h_{lv} = 850,530$ J/kg. The advancing (θ_a) and receding (θ_r) contact angles were taken as these of Ethanol with a particular stainless-steel sample of roughness $Ra = 0.4$ μ m, having values of 19° and 18°, respectively.

For the first series of numerical simulations, in order to observe the effects of channel aspect ratio at different heat fluxes, the overall analysis for all of the three considered channel aspect ratio values, was performed for three different values of applied heat flux, $q'' = 20, 50$ and 100 kW/m² and three different liquid velocities at the inlet (indicated as low, medium and high). For the second series of numerical simulations only the lowest heat flux and mass flux for each channel aspect ratio are considered. The overall details regarding the different channel aspect ratio cases considered for each of the main two series of numerical simulations are summarised in Tables 1 and 2, respectively.

Table 1. Considered channel aspect ratios and corresponding mass flow rates for Series 1 of numerical simulations (these cases are considered for $q'' = 20, 50$ and 100 kW/m²).

Series 1		W [mm]	H [mm]	D _h [mm]	β	G [kg/m ² s]	U _l [m/s]
I	a	0.15	0.30	0.20	0.5	73.7	0.10
	b					149.6	0.20
	c					294.7	0.40
II	a	0.20	0.20	0.20	1.0	98.2	0.13
	b					199.5	0.27
	c					392.9	0.53
III	a	0.35	0.14	0.20	2.5	171.9	0.23
	b					349.1	0.47
	c					687.6	0.93

Table 2. Considered channel aspect ratios and corresponding mass flow rates for Series 2 of numerical simulations (these cases are considered only for $q'' = 20$ kW/m²).

Series 2	W [mm]	H [mm]	D _h [mm]	β	\dot{m} [kg/m ² s]	U _l [m/s]
I	0.15	0.30	0.20	0.5	73.7	0.10
II	0.20	0.20	0.20	1.0	98.2	0.13
III	0.35	0.14	0.20	2.5	171.9	0.23

3.3 Computational Resources

A High-Performance Computing (HPC) cluster was utilised for a total of 54 runs. Each run required 200 computational cores. The duration of the computation for each of the 27 single phase simulations (one for each combination of q'' , G and β values) was approximately 10 days, as a few seconds of real flow were required for a steady state condition to be reached. For the corresponding 27 two-phase simulations, the duration of the computation was only three days since just a few milliseconds of real flow were required for the generated vapour bubble to reach the outlet of the channel. In total, 1,680,000 core-hours were utilised for the final runs of Series 1 numerical simulations. For the Series 2 of numerical simulations (multiple initial bubble seeds), only the lowest mass flux and heat flux were considered. In this case, the same stage 1 simulations with the corresponding Series 1 runs were used as initial condition, but more than one bubble seeds were patched in the conjugate heat transfer boundary at the beginning of the second stage of two-phase flow runs. Therefore, only three, in total, two-phase flow simulations were considered for a total real flow time of a few milliseconds. These were also run utilising 200 computational cores each and the total calculation time for each one was 3 days. Therefore, a total of additional 43,200 core-hours was utilised for the final runs of Series 2 numerical simulations that are presented in the present paper. It should be mentioned that a variable calculation time step was utilised for all runs with the courant number kept constant at 0.5 for the two-phase simulations and 1.0 for the single-phase simulations. Hence, for the two-phase simulations, the calculation time step was varied automatically, ranging from approximately 10^{-8} up to 10^{-6} s.

4. Single bubble seed numerical simulations

The spatial and temporal evolution of the generated vapour bubbles for Cases Ib, IIb and IIIb, of Table 1, for an applied heat flux value of $q'' = 20\text{kW/m}^2$, is depicted, indicatively, in Figure 3. The grey semi-transparent surface represents the liquid/vapour interface, while the coloured contours in a clip section that extends from one side of the channel up to its middle plane, reveals the instantaneous temperature fields in both the fluid and solid regions of the computational domain. The equivalent bubble diameter, calculated as a sphere with the same volume, is indicated for each time instance.

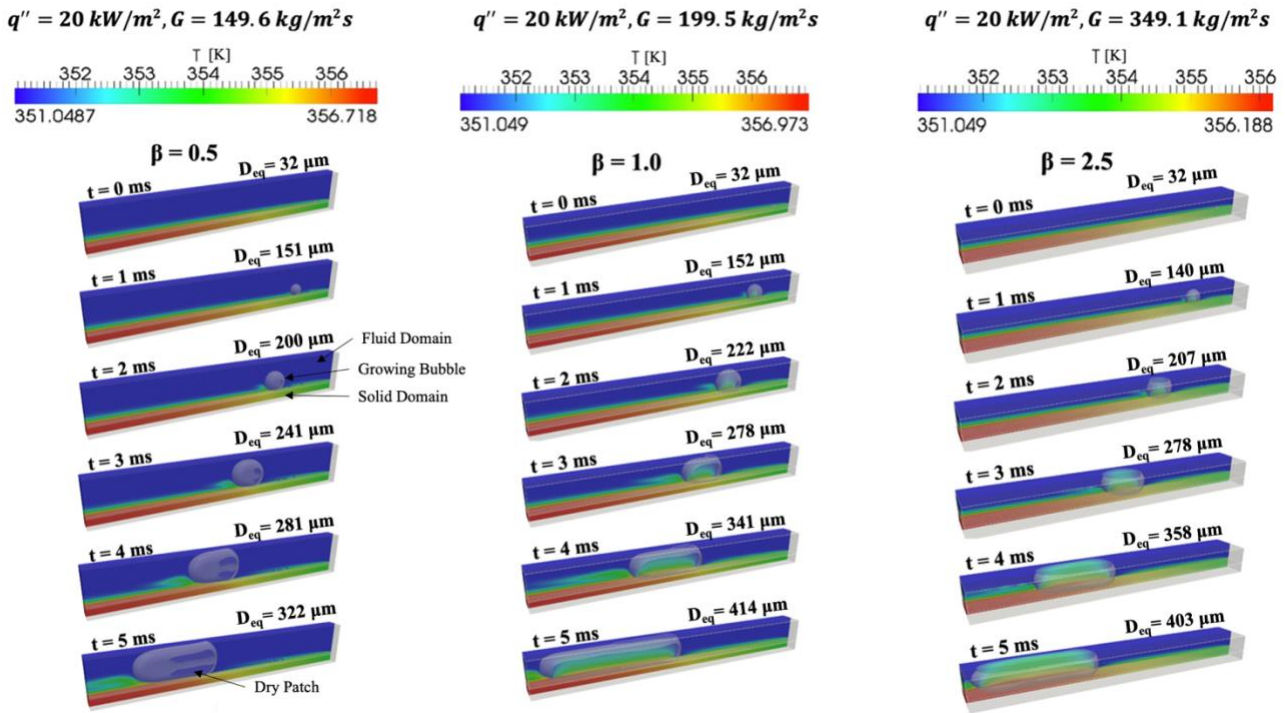


Figure 3. The spatial and temporal evolution of the generated vapour bubble ($q'' = 20 \text{ kW/m}^2$ and $G = 149.6, 199.5$ and $349.1 \text{ kg/m}^2\text{s}$ for $\beta = 0.5, 1.0$ and 2.5 , respectively).

It is evident that the variation of the channel aspect ratio has a quite significant effect in the resulting bubble growth dynamics. For $\beta = 0.5$, the bubble grows into a Taylor bubble maintaining minimal contact with the channel walls, with a liquid film formed between the bubble and the channel walls, apart from some small dry patches at the side walls. For $\beta = 2.5$, the bubble grows into an elongated vapour slug that maintains in contact with the top and bottom walls of the channel, throughout most of its length. However, no dry patches at the side walls are observed in this case. Therefore, for $\beta = 0.5$, the bubble grows mainly due to liquid film evaporation, while for $\beta = 2.5$ the bubble grows due to vapour/liquid/solid contact line evaporation. In the case of $\beta = 1.0$, the generated bubble grows into an elongated vapour slug that maintains continuous contact with the bottom heated boundary almost for its entire length, while some minimal contact with the top boundary is evident after $t=3$ ms without however, this contact extending for the entire length as in the case of the bottom boundary of the fluid domain. Dry patches with the side walls of the microchannel are also evident that extend almost for the entire length of the bubble, after $t=3$ ms. Therefore, also in this case, since there is no liquid film formed at the vicinity of the bottom heated wall, the dominant heat transfer mechanism is only the contact line evaporation. As expected, in all three cases, due to the associated latent heat of evaporation, as the bubble grows and moves towards the outlet, the temperature of the heated solid domain is decreasing since the solid domain cools down.

In Figures 4 and 5, the corresponding temporal and spatial bubble evolution is also shown, once more for the medium velocity (i.e., mass flux) cases, Cases Ib, IIb and IIIb, of Table 1, for applied heat flux values of 50 kW/m^2 and 100 kW/m^2 , respectively.

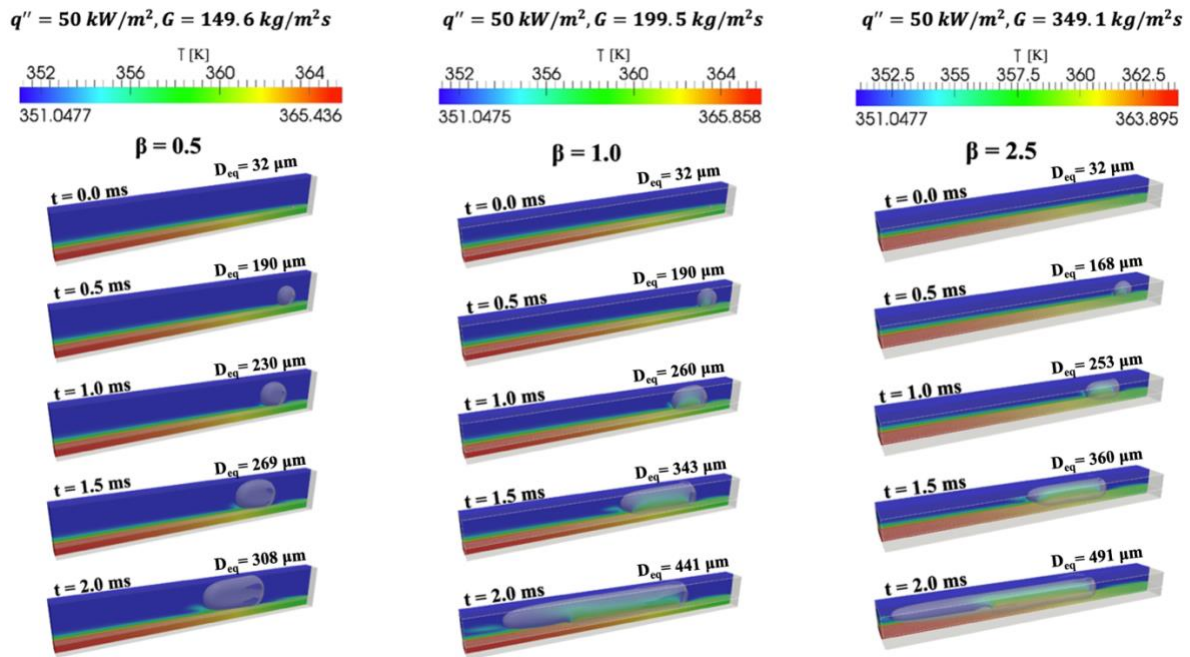


Figure 4. The spatial and temporal evolution of the generated vapour bubble ($q'' = 50 \text{ kW/m}^2$ and $G = 149.6, 199.5$ and $349.1 \text{ kg/m}^2\text{s}$ for $\beta = 0.5, 1.0$ and 2.5 , respectively).

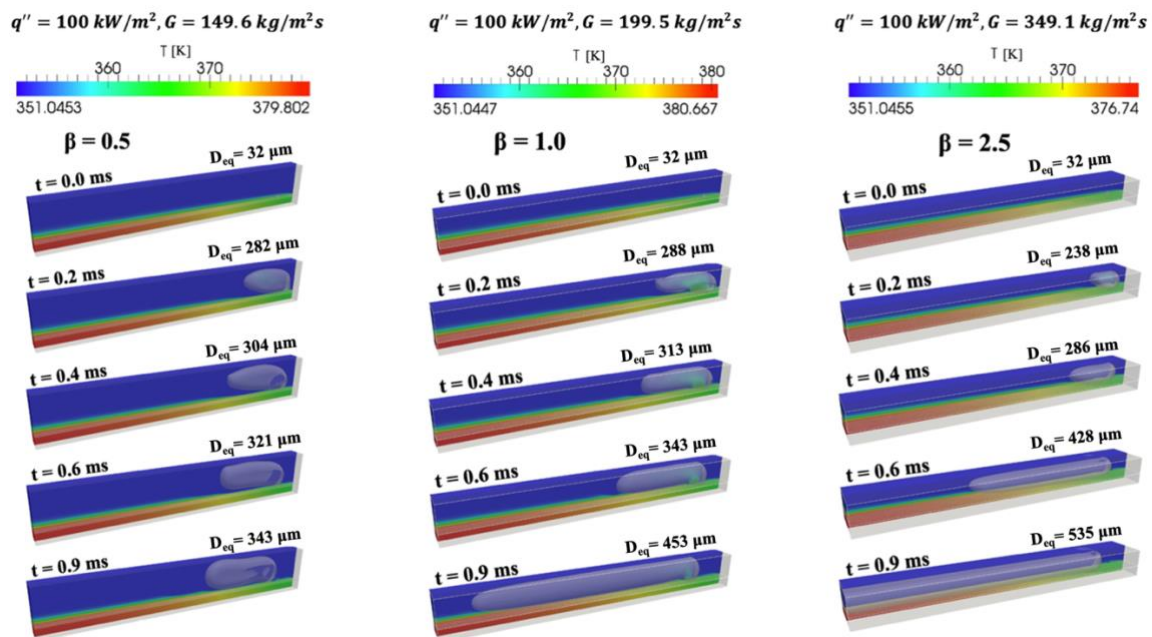


Figure 5. The spatial and temporal evolution of the generated vapour bubble ($q'' = 100 \text{ kW/m}^2$ $G = 149.6, 199.5$ and $349.1 \text{ kg/m}^2\text{s}$ for $\beta = 0.5, 1.0$ and 2.5 , respectively)

It is evident that the previous observations still hold for the $\beta = 0.5$ cases, as the applied heat flux subsequently increases. Also, for the higher β applied heat fluxes, the bubble grows into a Taylor bubble maintaining minimal contact with the channel walls, with a liquid film formed between the bubble and the channel walls, apart from some small dry patches at the side walls. It is, however, obvious that with the subsequent increase in the heat flux, the generated bubble reaches at a similar volume at much earlier flow times, which indicates a subsequent increase in the evaporation rates ($t=5.0 \text{ ms}$ for $q''=20 \text{ kW/m}^2$, $t=2.0 \text{ ms}$ for $q''=50 \text{ kW/m}^2$ and $t=0.9 \text{ ms}$ for $q''=100 \text{ kW/m}^2$). For the cases of $\beta = 1.0$ and $\beta = 2.5$ and for $q''=50 \text{ kW/m}^2$, it is observed that the increase in the applied heat

flux from $q''=20 \text{ kW/m}^2$ to $q''=50 \text{ kW/m}^2$ leads to the development of a liquid film at the later stages of the bubble development that extends from the leading edge of the elongated bubble up to a quite significant portion upstream ($t=2.0 \text{ ms}$, $\beta = 1.0, 2.5$). This development of the liquid film for $\beta = 1.0$ and $\beta = 2.5$ is further enhanced with the further increase of the applied heat flux to $q''=100 \text{ kW/m}^2$. As it can be seen, the liquid film development for $q''=100 \text{ kW/m}^2$ starts much earlier ($t=0.2 \text{ ms}$) for both $\beta = 1.0$ and $\beta = 2.5$ than in the corresponding cases of $q''=50 \text{ kW/m}^2$ ($t=1.5 \text{ ms}$). Summarising, it is evident that also for higher values of applied heat flux, the variation of the channel aspect ratio has a quite significant effect in the resulting bubble growth dynamics. It is also evident that as the applied heat flux increases, the liquid film evaporation starts to become progressively more dominant for higher aspect ratio channels.

The effect of the variation of the applied liquid mass flux at the channel inlet on the generated vapour slug dynamics is indicatively shown for the lowest of the considered applied heat fluxes ($q''=20 \text{ kW/m}^2$) and for all three considered aspect ratios, in Figures 6, 7 and 8.

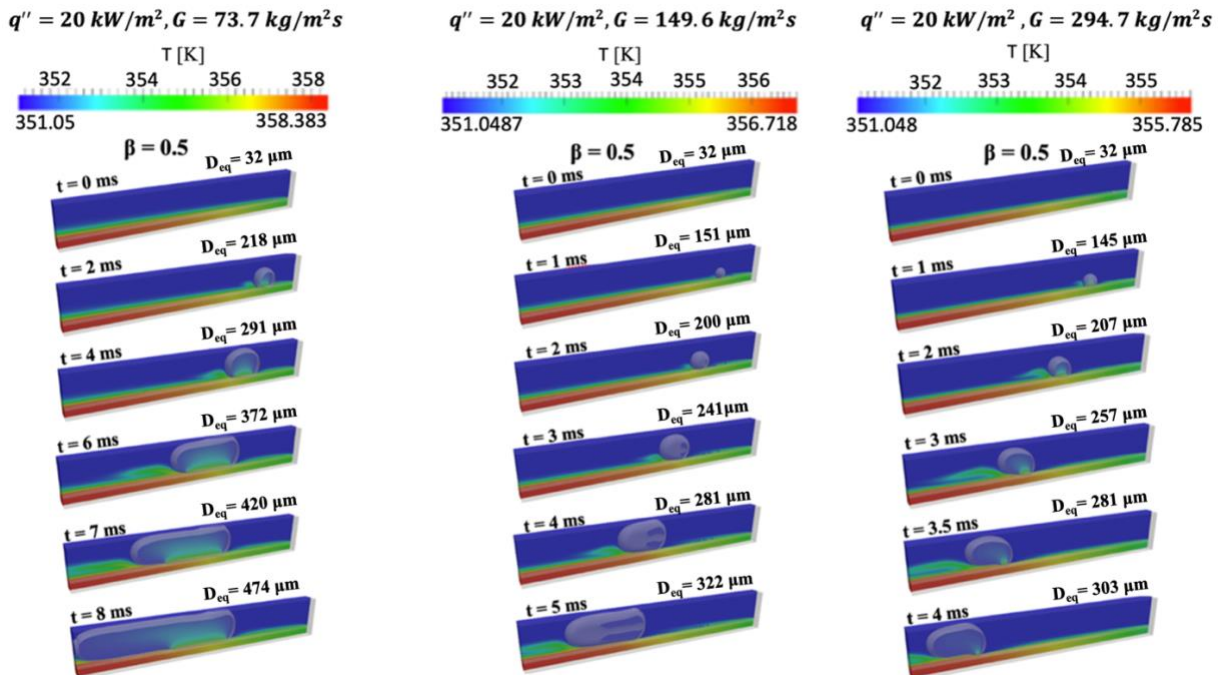


Figure 6. The spatial and temporal evolution of the generated vapour bubble ($q'' = 20 \text{ kW/m}^2$, $\beta = 0.5$ and $G = 73.7, 149.6, 294.7 \text{ kg/m}^2\text{s}$).

As it can be observed, the area of the dry patches with the side walls that was already observed in the medium mass flux case is enhanced at lower and higher mass fluxes for $\beta = 0.5$. Moreover, for both lower and higher mass fluxes a direct contact of the generated bubble with the bottom heated wall is observed. Therefore, it is obvious that for $\beta = 0.5$ and for low and high mass fluxes, contact line evaporation also occurs in combination with the liquid film evaporation that was dominant in the case of the medium mass flux. However, in all of the examined mass fluxes, liquid film evaporation appears to be the prevailing heat transfer mechanism for $\beta = 0.5$. Finally, in general, it is evident that the increase of the mass flux leads to a subsequent decrease in the vapour slug volume that reaches

the outlet of the micro-channel. This is due to the higher traveling speed of the generated bubble and hence, the resulting less time that it experiences evaporation.

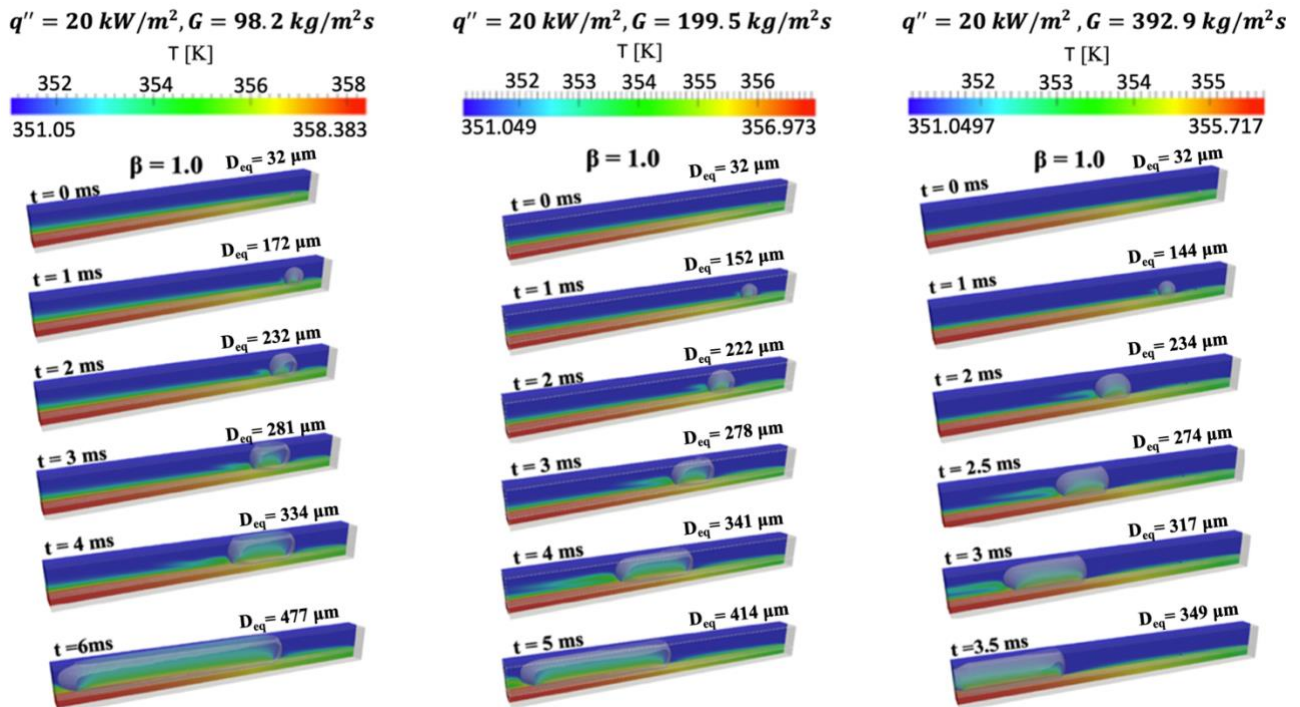


Figure 7. The spatial and temporal evolution of the generated vapour bubble ($q'' = 20 \text{ kW/m}^2$, $\beta = 1.0$ and $G = 98.2, 199.5, 392.9 \text{ kg/m}^2\text{s}$).

For $\beta = 1.0$, the decrease of the applied mass flux leads to a considerable increase of the contact area of the vapour slug with the top wall of the channel, in comparison to what is observed for the medium mass flux value. The dry patch areas with the side walls are, however, similar for low and medium mass fluxes. On the other hand, the increase of the mass flux leads to a delay in the development of the dry patches with the top and the side walls of the channel. For all three of the considered mass fluxes contact line evaporation seems to be the prevailing heat transfer mechanism for $\beta = 1.0$. Finally, also for $\beta = 1.0$, the increase of the mass flux leads to a subsequent decrease in the vapour slug volume that reaches the outlet of the considered microchannel.

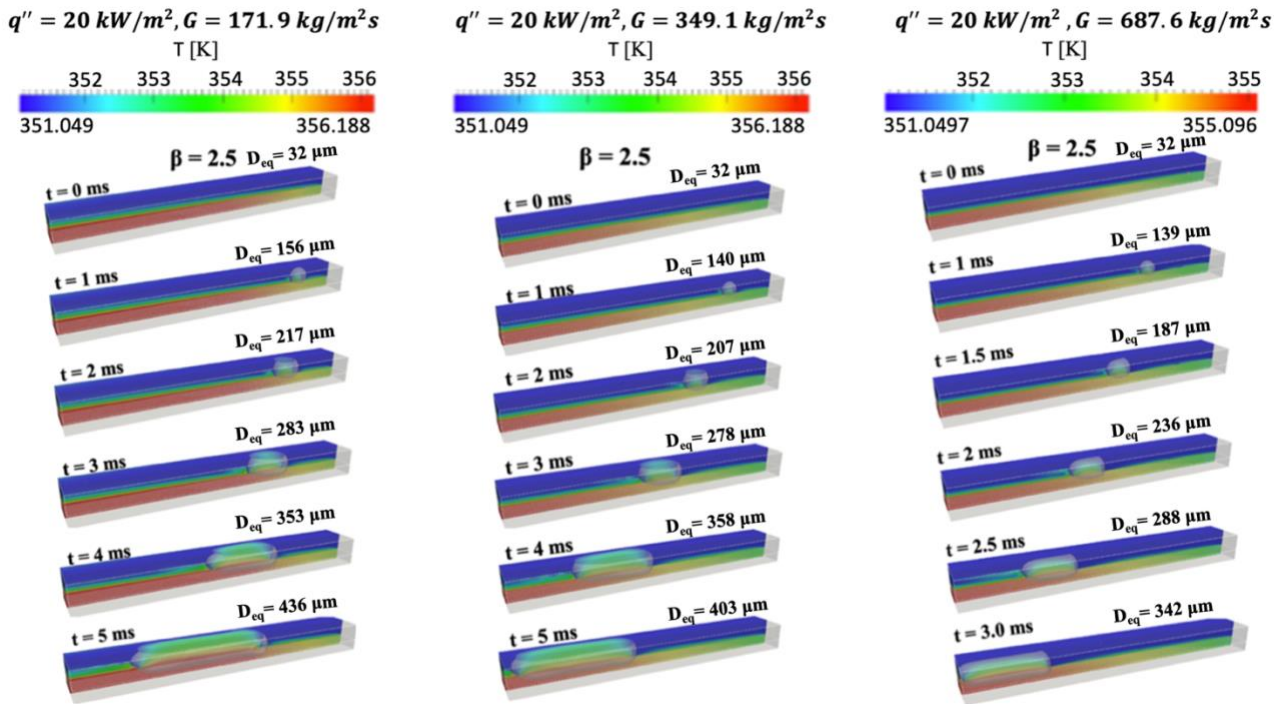


Figure 8. The spatial and temporal evolution of the generated vapour bubble ($q'' = 20 \text{ kW/m}^2$, $\beta = 2.5$ and $G = 171.9, 349.1, 687.6 \text{ kg/m}^2\text{s}$).

For $\beta = 2.5$, the decrease of the applied mass flux appears to have a negligible effect in the generated vapour slug dynamics. Both for low and medium mass fluxes, the bubble grows into an elongated vapour slug that maintains contact with the top and bottom walls of the channel throughout most of its length, without any dry patches developing at the side walls of the microchannel. However, for the higher mass flux value, the bubble appears to be in contact only with the bottom wall without any dry patches developing at the top and side walls. For all three of the considered mass fluxes, contact line evaporation is the prevailing heat transfer mechanism also for $\beta = 2.5$.

In order to identify and quantify the effects of channel aspect ratio on the local, instantaneous heat transfer, in Figure 9, the instantaneous local Nusselt number $Nu(x)$ is plotted over the dimensionless length $L^* = x/L$ of the considered microchannel, along the central longitudinal axis of the conjugate heat transfer boundary, for the three considered channel aspect ratios, for all values of the applied heat flux and for the medium of the examined mass fluxes, for three successive time instances in each case, respectively. In all cases, also the corresponding single-phase curve from the initial condition (Stage 1 simulations) of the corresponding two-phase simulation stages (Stage 2 simulations) is plotted as a reference. The local heat transfer coefficient is first calculated as the ratio of the applied heat flux over the temperature difference between the heated wall temperature and the saturation temperature, $h(x) = \frac{q''}{T_w(x) - T_{sat}}$, and then, the local Nusselt number is calculated as the ratio of the product of the heat transfer coefficient with the channel hydraulic diameter over the thermal conductivity of the liquid, $Nu(x) = \frac{h(x)D_h}{\lambda_l}$.

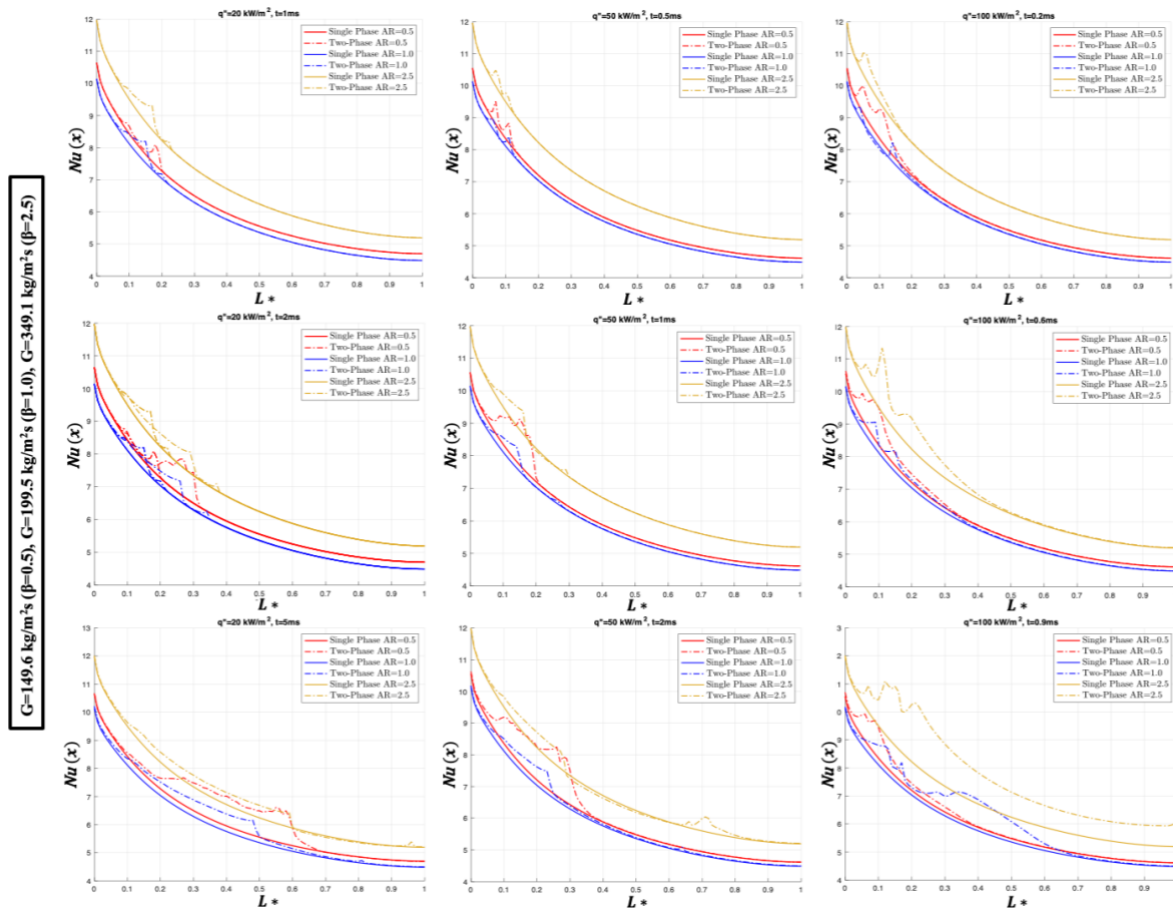


Figure 9. Effect of the aspect ratio (β) on the local instantaneous Nusselt number ($Nu(x)$) along the conjugate heat transfer boundary as a function of dimensionless length (L^*), for different applied heat fluxes ($q'' = 20, 50, 100 \text{ kW/m}^2$) and the medium in each case applied mass flux ($G = 149.6 \text{ kg/m}^2\text{s}$ for $\beta=0.5$, $G = 199.5 \text{ kg/m}^2\text{s}$ for $\beta=1.0$, $G = 349.1 \text{ kg/m}^2\text{s}$ for $\beta=2.5$).

Focusing on the single-phase curves, it can be observed that the initial increase of β from 0.5 to 1.0, results in slightly lower values of $Nu(x)$ along the heated wall. However, the further increase of β to 2.5 results in a significant increase in the values of $Nu(x)$, indicating an enhancement in the local heat transfer coefficient, for all the examined heat fluxes. Examining now the resulting $Nu(x)$ for the two-phase flow stages, it can be observed that, for all three values of the applied heat flux, at the early stages of the bubble growth (time $t = 1.0 \text{ ms}$ for $q'' = 20 \text{ kW/m}^2$, $t = 0.5 \text{ ms}$ for $q'' = 50 \text{ kW/m}^2$ and $t = 0.2 \text{ ms}$ for $q'' = 100 \text{ kW/m}^2$), two successive peaks in the $Nu(x)$ values are encountered in comparison with the corresponding single-phase curves. These are due to the contact line evaporation at these points along the conjugate heat transfer boundary.

As the bubble growth process continues (time $t = 2.0 \text{ ms}$ for $q'' = 20 \text{ kW/m}^2$, $t = 1.0 \text{ ms}$ for $q'' = 50 \text{ kW/m}^2$ and $t = 0.6 \text{ ms}$ for $q'' = 100 \text{ kW/m}^2$), for the narrow microchannel ($\beta = 0.5$), where the bubble maintains a minimal contact area with the heated wall, with a successively developing liquid film region, the local heat transfer is significantly enhanced due to liquid film evaporation, approaching local instantaneous Nu values similar to the wide microchannel ($\beta = 2.5$). In this case, it is characteristic that an enhanced local heat transfer zone is traced also upstream of the bubble

position that gradually attenuates towards the inlet of the channel. As for the square ($\beta = 1.0$) and wide microchannels ($\beta = 2.5$), where the growing bubbles maintain a significant contact area with the conjugate heat transfer boundary, a local increase of the instantaneous Nu number (with respect to the single-phase curves) is observed, at the points where the central wall longitudinal axis (sampling line) meets the contact line between the bubble interface and the heated wall. Also, in these cases, upstream of the first peak point, an enhanced region of local heat transfer is traced that gradually attenuates to the single-phase values towards the inlet. This is due to the thermal inertia of the solid domain. In more detail, as the bubble grows and moves towards the microchannel outlet, due to either contact line evaporation or liquid film evaporation or due to a combination of these two mechanisms, the solid wall temperature is reduced significantly, resulting to an increase in the local heat transfer coefficient, due to the resulting reduction in the temperature difference between the wall of the channel and the saturation temperature. However, due to the thermal inertia of the solid wall, it takes some time for the wall temperature to increase again. This has as a result the development of this region of enhanced local heat transfer, behind the moving bubbles. The same behaviour is observed also for the later stages of the bubble growth process (time $t = 5.0$ ms for $q'' = 20$ kW/m², $t = 2.0$ ms for $q'' = 50$ kW/m² and $t = 0.9$ ms for $q'' = 100$ kW/m²). For $q'' = 100$ kW/m², liquid films have been developed for all three of the considered aspect ratios, leading to a significant enhancement of the local heat transfer.

From all these observations, it is evident that the variation of the aspect ratio of a microchannel has a significant effect in the local heat transfer coefficient, due to an enhancement in the single-phase heat transfer, combined with the alteration of the underpinned bubble growth dynamics (when boiling occurs and a two-phase flow is developed), that may result in different contributions of contact line versus liquid film evaporation. Furthermore, it is shown that the thickness and thermal properties of the channel walls have a major impact on the local instantaneous heat transfer, due to the associated thermal inertia of the solid domains. This last conclusion highlights the importance of considering Conjugate Heat Transfer simulations for flow boiling investigation within micro-passages and constitutes one of the main novelties of the present numerical investigation.

For practical applications, since the time averaged local heat transfer is more meaningful than the instantaneous one for microchannel heat sinks design, in Figure 10, the effect of the channel aspect ratio on the time-averaged local Nusselt number is plotted for all of the considered heat and mass flux levels. In each case, the corresponding initial condition curve (from the steady state, single-phase stage of the conducted simulations) is also plotted for reference.

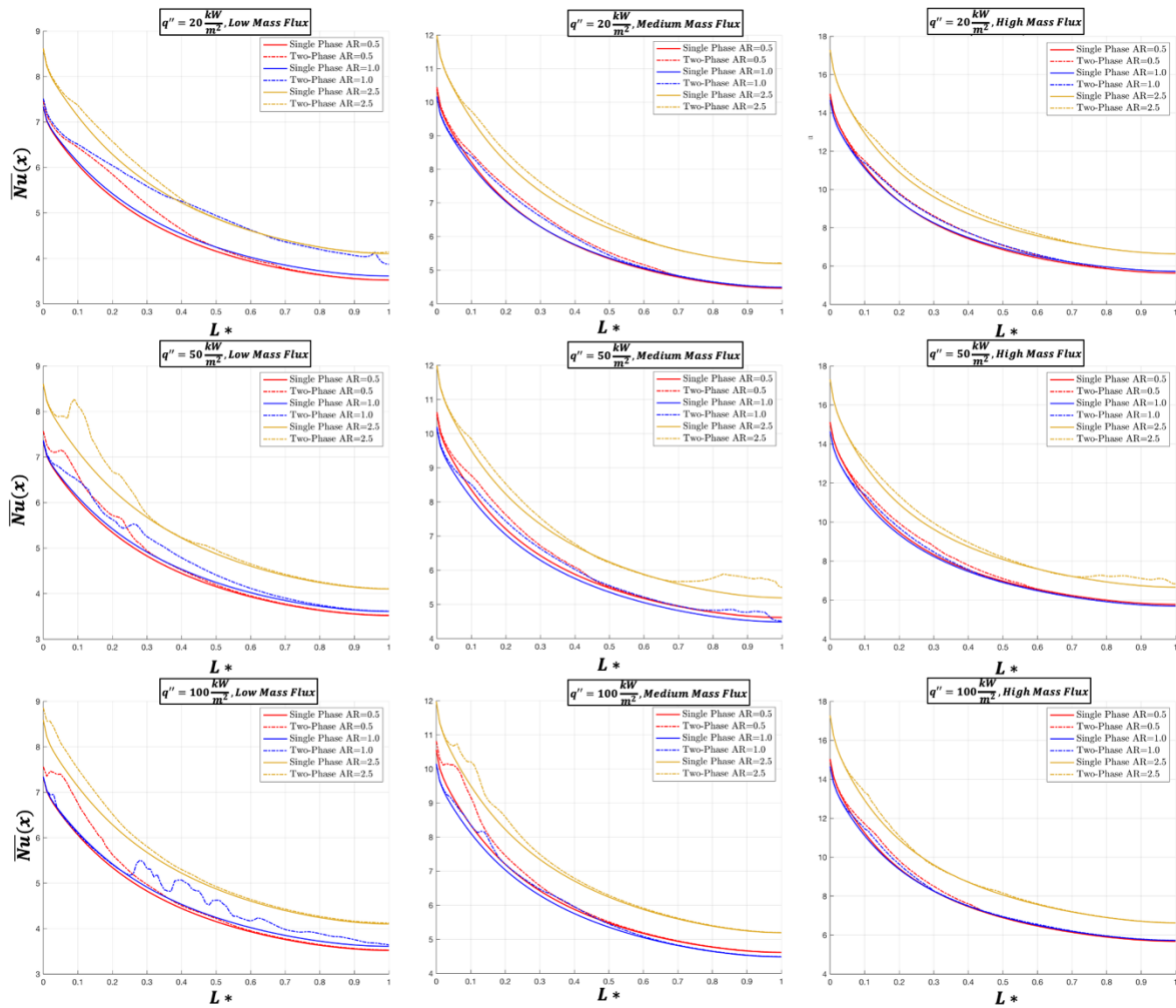


Figure 10. Effect of the aspect ratio (β) on the local time averaged Nusselt number ($\overline{Nu}(x)$) along the conjugate heat transfer boundary as a function of dimensionless length for different mass fluxes (low, medium, high) and heat fluxes (20 kW/m^2 , 50 kW/m^2 and 100 kW/m^2), using a single nucleation site.

As it can be observed, in general, for all combinations of applied heat flux and mass flux, the channel with $\beta=2.5$ results in significantly higher Nusselt values in comparison to the other two values of aspect ratio ($\beta=0.5$ and $\beta=1.0$), which show comparable heat transfer performance for most of the heat flux and mass flux combinations. However, this can be mainly attributed to the significantly higher single-phase stage heat transfer for the channel with $\beta=2.5$, with respect to the channels with $\beta=0.5$ and $\beta=1.0$ which both start from a similar initial condition. It is also obvious that for all the applied heat fluxes, and all the considered aspect ratios, the increase of the mass flux results in a subsequent decrease in the two-phase time-averaged local Nusselt number values. On the contrary, the increase of the applied heat flux does not seem to have a significant influence of the resulting two-phase Nusselt numbers, with respect to the single-phase stage curves. Just a local redistribution of the regions of higher Nusselt numbers, with respect to the corresponding single-phase curves, is observed with the increase of the applied heat flux, especially for the lower and medium mass fluxes.

To further quantify the effect of the channel aspect ratio variation, Table 3 summarises the average and the maximum differences of the two-phase time-averaged Nusselt numbers, from the corresponding single-phase stage curves as well as the global Nusselt number, calculated as the area under the two-phase flow curves, for all the considered aspect ratios and applied heat flux and mass flux combinations. As it can be observed more clearly from the global Nusselt numbers, for all applied heat flux values and mass flux levels combinations, the channel with aspect ratio of $\beta=2.5$ shows the highest heat transfer performance, while the other two channels with aspect ratios of $\beta=0.5$ and $\beta=1.0$ show a quite similar heat transfer performance.

Table 3. Average and maximum differences of two-phase time averaged Nusselt numbers from the corresponding single-phase stage curves, and global Nusselt number of two-phase simulation stages, for all the considered aspect ratio, applied heat flux and mass flux combination (single nucleation site cases).

Case	β	q'' [KW/m ²]	G [kg/m ² s]	Average difference between single- phase and two- phase curves (%)	Maximum difference between single- phase and two- phase curves (%)	Nu _{glob}
1	0.5	20	low	3.225	9.436	4.66
2	1	20	low	12.142	16.535	5.11
3	2.5	20	low	1.285	4.355	5.35
4	0.5	50	low	2.538	10.789	4.63
5	1	50	low	3.123	9.124	4.73
6	2.5	50	low	2.407	14.560	5.42
7	0.5	100	low	2.937	13.695	4.66
8	1	100	low	3.918	11.835	4.74
9	2.5	100	low	1.978	6.861	6.86
10	0.5	20	medium	2.768	6.650	6.04
11	1	20	medium	1.858	4.989	5.98
12	2.5	20	medium	1.493	3.760	6.94
13	0.5	50	medium	2.011	5.961	6.15
14	1	50	medium	4.026	6.250	6.09
15	2.5	50	medium	3.257	10.674	7.03
16	0.5	100	medium	2.071	12.201	6.17
17	1	100	medium	1.670	6.703	5.97
18	2.5	100	medium	1.550	8.115	6.96
19	0.5	20	high	2.237	4.910	7.87
20	1	20	high	1.747	4.251	7.86
21	2.5	20	high	1.587	3.956	9.14
22	0.5	50	high	1.782	5.460	7.97
23	1	50	high	1.091	3.960	7.79
24	2.5	50	high	2.561	6.409	9.22
25	0.5	100	high	1.401	5.723	7.86
26	1	100	high	0.841	4.269	7.80
27	2.5	100	high	0.621	4.195	9.05

5. Multiple Bubble Seeds Numerical Simulations

From the analysis and comparison of all considered cases so far, it is evident that the variation of the channel aspect ratio directly affects the resulting generated bubble dynamics that, in turn, has a

noticeable effect on the resulting local and global heat transfer characteristics. However, since during flow boiling in micro-channels, usually multiple nucleation sites are activated simultaneously, and there could be bubble to bubble interactions that might additionally affect the developing two-phase flow regime and, therefore, the heat transfer characteristics, three additional cases are considered in the present investigation.

In more detail, for the lowest of the examined heat fluxes and mass fluxes for each aspect ratio (worst case scenario from the heat transfer performance point of view), an additional simulation is performed, starting from the same initial single-phase flow stages as before, patching this time 30 arbitrary distributed bubble nuclei along the conjugate heat transfer boundary. The proposed simulations use the same parameters as the corresponding ones previously presented, where the applied heat flux is $q'' = 20 \text{ kW/m}^2$ and the applied mass fluxes are $G = 73.7, 98.2$ and $171.9 \text{ kg/m}^2\text{s}$, for the channels with aspect ratio $\beta = 0.5, 1.0$ and 2.5 , respectively. The radius of the 30 initialised bubble nuclei is $20\mu\text{m}$, and their position remains the same with respect to the central longitudinal axis of the conjugate boundary in all three channels.

Figure 11 shows the spatial and temporal evolution of the 30 initiated bubble seeds for the first 1.3 ms from their initiation. As expected, the bubble seeds evaporate, grow, and coalesce. In all three cases, apart from an initial part in the vicinity of the channel inlet, from the early stages ($t = 0.4 \text{ ms}$), the initial bubble seeds have grown significantly and merged into an elongated vapour slug that extends from the outlet of the channel up to a certain upstream point, a bit after the middle of the channel for the channels with aspect ratios $\beta = 0.5$ and 1.0 , and a bit before the middle point of the channel for the channel with aspect ratio $\beta = 2.5$. From the inlet up to the proposed point, smaller bubbles, in a slug plug flow arrangement, are observed in all cases. The size of these upstream bubbles appears smaller in the case of $\beta = 2.5$ than in the cases of $\beta = 0.5$ and 1.0 , where the proposed bubbles are of comparable size. However, it is evident that the aspect ratio has a considerable effect in the shape and form of the generated bubbles. In more detail, for $\beta = 0.5$, the generated bubbles maintain a contact with the conjugate boundary (bottom heated wall) as well as with the side vertical channel walls, for the entire 1.2 ms that are considered here. With the increase of the aspect ratio to $\beta = 1.0$, not any contact with the side walls is observed and only a small contact area with the conjugate boundary is evident. Finally, in the case of the channel with aspect ratio $\beta = 2.5$, apart from the contact with the bottom heated wall, a significant contact area with the top channel wall is also evident.

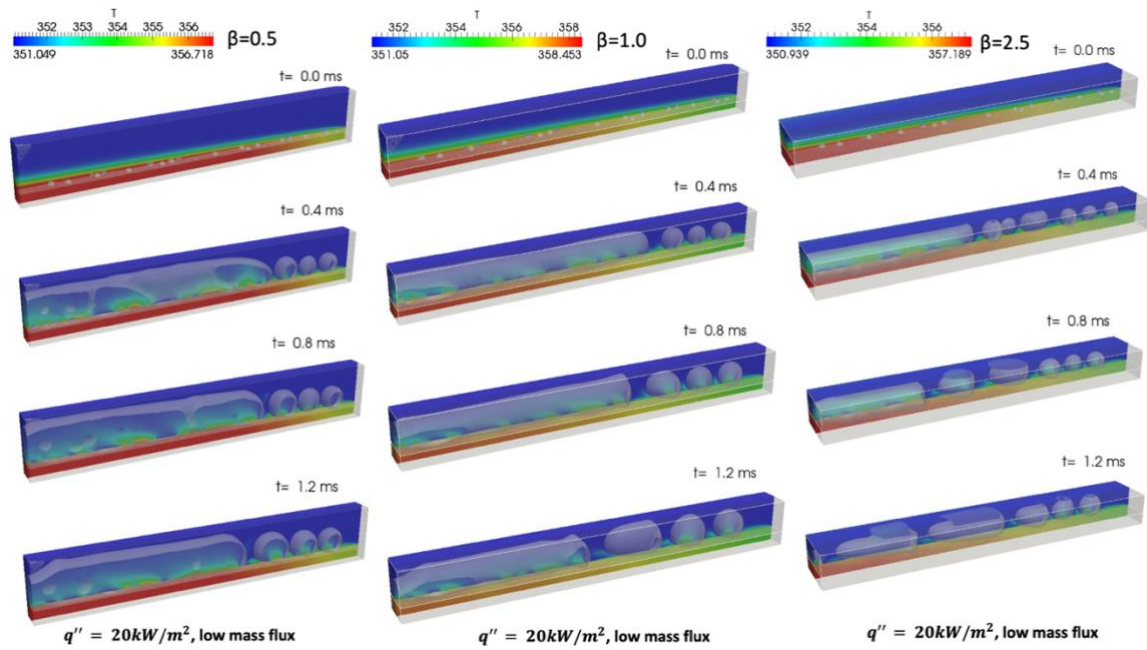


Figure 11. The spatial and temporal evolution of the generated vapour bubbles, $q'' = 20 \text{ kW/m}^2$, and $G = 73.7$ ($\beta = 0.5$), 98.2 ($\beta = 1.0$) and 171.9 ($\beta = 2.5$) $\text{kg/m}^2\text{s}$.

To reach a more quantitative comparison, the time-averaged local Nusselt number along the dimensionless length of the channel is plotted for each channel aspect ratio (dashed lines), in Figure 12. The initial single-phase stage curves for each case are also plotted for reference (solid lines).

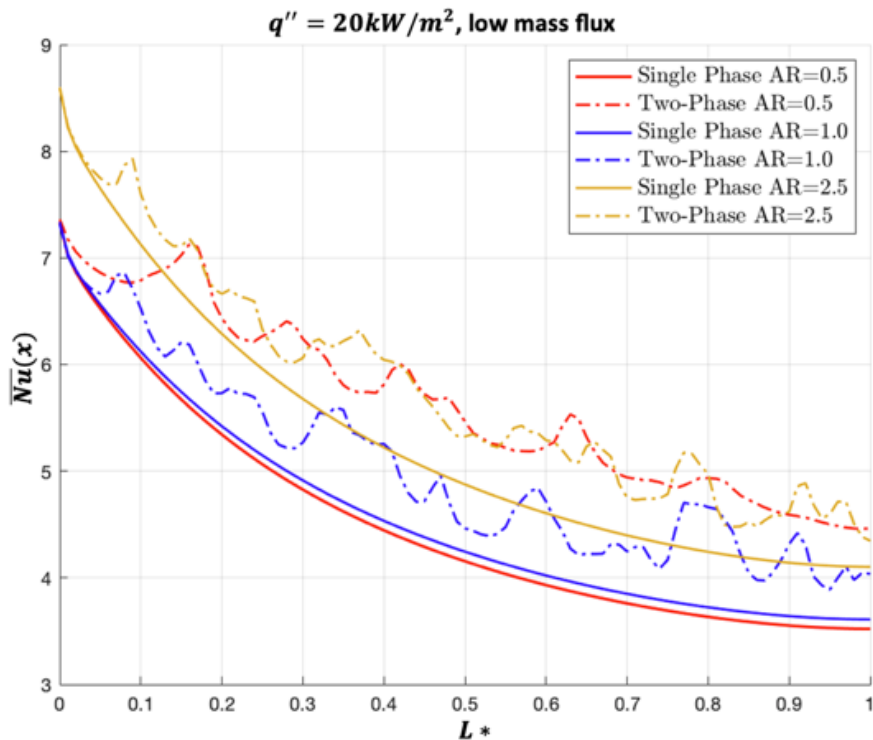


Figure 12. Effect of the aspect ratio (β) on the local time averaged Nusselt number ($\overline{Nu}(x)$) along the conjugate heat transfer boundary as a function of dimensionless length for low mass fluxes and a heat fluxes of 20 kW/m^2 , using multiple simultaneous nucleation sites.

As it can be observed, in all three cases, the increase of the Nusselt number, in comparison to the single-phase stage curves, is significantly higher than in the corresponding single nucleation site cases (Figure 10). What is interesting is that, in the case of multiple nucleation sites, the two-phase flow curve of the channel with aspect ratio $\beta = 0.5$ shows comparable levels of local Nusselt number along the channel length, with respect to $\beta = 2.5$, even though the Nu at the initial single-phase stage of the simulations is significantly lower for $\beta = 0.5$. This was not evident in the single nucleation site runs (Figure 10), where the $\beta = 2.5$ channel showed significantly higher local time averaged Nusselt numbers than the other two channels with $\beta = 0.5$ and $\beta = 1.0$, which resulted in comparable to each other values. This is also evident comparing the Global Nusselt Numbers for each of the three cases which are summarised in Table 4. Table 4 also reports the average and maximum % difference between the single-phase flow initial stage and two-phase flow curves. It is evident that the channel with aspect ratio $\beta = 0.5$ show significantly higher both average and maximum % difference values, in comparison to the channels with aspect ratios $\beta = 1.5$ and $\beta = 2.5$, and, therefore, it results to a Global Nusselt number value that is quite close to the channel with aspect ratio $\beta = 2.5$.

Table 4. Average and maximum differences of two-phase time averaged Nusselt numbers from the corresponding single-phase stage curves, and global Nusselt number of two-phase simulation stages, for all the considered aspect ratios, applied heat flux $q'' = 20 \text{ kW/m}^2$ and low mass flux values $G = 73.7$ ($\beta = 0.5$), 98.2 ($\beta = 1.0$) and 171.9 ($\beta = 2.5$) $\text{kg/m}^2\text{s}$ (single nucleation site cases).

Case	β	q'' [KW/m ²]	G [kg/m ² s]	Average difference between single- phase and two- phase curves (%)	Maximum difference between single- phase and two- phase curves (%)	Nu _{glob} (Area under the two-phase curves)
1	0.5	20	low	27.13	42.78	5.64
2	1	20	low	10.57	25.59	5.02
3	2.5	20	low	10.42	20.92	5.78

At this point, it should also be mentioned that, as it was shown in a previous investigation [28], where the effect of wettability for a channel aspect ratio of $\beta = 0.5$ was investigated, the observed maximum and average percentage increase of the time-averaged local Nusselt number, in comparison to the initial single phase stage of the simulation as well as the global Nusselt number, can be further increased to even higher values, for the case of recurring nucleation events from multiple nucleation sites.

6. Conclusions

In the present paper, a fundamental analysis on the effect of the channel aspect ratio on the bubble dynamics and heat transfer characteristics at the early transient stages of the bubble growth within confined microchannels, under saturated flow boiling conditions, is conducted. According to the Authors' best knowledge, this is the first time that an investigation is focusing on the effect of the

channel aspect ratio variation on the first transient stage of the bubble growth and heat transfer characteristics, illustrating the importance of this transient stage to the bubble growth dynamics as well as the underpinned heat transfer characteristics and mechanisms. A previously developed and validated, custom, enhanced, diabatic version of the VOF method in OpenFOAM, that accounts for spurious velocities dampening, accurate dynamic contact angle modelling, phase-change due to boiling and condensation, as well as conjugate heat transfer between solid and two-phase fluid domains, is utilised for this purpose. Different applied heat fluxes and mass fluxes were tested for each of the three considered channel aspect ratios. Ethanol was selected as the working fluid for all cases. Two different series of numerical simulations were conducted. In the first series, only a single nucleation event from a single nucleation site is considered to examine the effect of the channel aspect ratio on a single vapour slug development, trying to identify the prevailing heat transfer mechanism in each case, i.e., contact line versus liquid film evaporation. In the second series, multiple arbitrary located nucleation sites are used for the lower value of the applied heat fluxes from the first series of simulations as well as for the lower level of applied mass fluxes in each case, to perform three more realistic scenarios with 30 arbitrary distributed simultaneous nucleation sites.

From the first series of numerical simulations, the following conclusions can be drawn:

- For low heat fluxes, the narrow microchannel ($\beta=0.5$), liquid film evaporation is the dominant heat transfer mechanism, while for the square ($\beta=1.0$) and wide ($\beta=2.5$) microchannels, contact line evaporation dominates and contributes to the cooling of the heated solid domain. As the applied heat flux increases, liquid film evaporation progressively becomes dominant also in the case of the square and wide microchannels. The applied mass flux appears to have a considerable effect in the generated bubble growth dynamics for the case of the narrow channel, since either lowering or increasing the mass flux leads to a combination of contact line and liquid film evaporation, since the contact areas of the generated bubble with the walls of the channel increase significantly. For the case of the square and wide microchannels, the variation of the mass flux does not alter the dominant heat transfer mechanism, which for all the examined mass fluxes is contact line evaporation.
- The aspect ratio of a microchannel has a significant effect on the local heat transfer characteristics. This happens due to an enhancement in the single-phase heat transfer, prior to the onset of nucleate boiling, combined with the alteration of the underpinned bubble growth dynamics and the resulting differentiation in the contributions of contact line versus liquid film evaporation, when boiling occurs and a two-phase flow is developed.

- The thickness and thermal properties of the solid channel walls have a major impact on the local instantaneous heat transfer, due to the associated thermal inertia of the solid domains.
- Comparing the global Nusselt numbers, it is also concluded that the wide microchannel shows indeed the highest heat transfer performance, however, this is mainly due to the single-phase flow stage contribution.

From the second series of numerical simulations, the following conclusions can be drawn:

- In all three examined channel aspect ratio cases, the initially arbitrary distributed bubble nuclei on the heated wall grow rapidly and merge, forming an elongated vapour slug that extends from the channel inlet up to an upstream point, close to the middle of the channel. From that point and further upstream towards the outlet, smaller bubbles with the slug-plug flow arrangement are developed.
- The length of the elongated vapour slug decreases with the increase of the channel aspect ratio. Moreover, the shape and form of both the elongated vapour bubble as well as of the smaller bubbles upstream (i.e., contact areas with the channel walls) is also affected significantly by the increase of the aspect ratio, indicating an alteration in the contribution of the dominant heat transfer mechanisms.
- From the comparison of the time-averaged local Nusselt numbers along the channels, it can be concluded that, for all cases, the increase of the Nusselt numbers is much higher when more realistic cases, with multiple simultaneous nucleation sites, are simulated, especially for the narrow channel. This leads to a similar overall heat transfer performance with respect to the wide channel, which was superior in the case of the isolated single bubble. This is also evident by comparing the resulting global Nusselt numbers.

From the overall analysis and discussion of the numerical simulation predictions of the present paper, the following more general conclusions can be drawn:

- The micro-passage aspect ratio has a significant effect in the generated bubble dynamics during the onset of the nucleate boiling regime, in the first transient period of the bubble growth and development within the confined liquid crossflow. This, in fact, regulates the size and position of the contact areas of the bubble with the microchannel walls, with a direct effect in the contribution and also the balance of the contact line versus liquid film evaporation.
- In general, the numerical simulations, which do not consider the conjugate heat transfer between solid and two-phase fluid domains, lead to poor results and should be avoided.

Acknowledgements

This research was partially funded through the European Union's Horizon 2020 research and innovation programme (Marie Skłodowska Curie grant agreement No. 801604), the European Space Agency (ESA MAP CORA projects TOPDESS and ENCOM4) and the UK's Engineering and Physical Science Research Council (grant EP/P013112/1). Dr. Andredaki would like also to thank the Advanced Engineering Centre of University of Brighton for the financial support through the Maintaining Continuity research grant scheme. Finally, Dr. Georgoulas would also like to thank University of Brighton specifically also for the financial support through the Rising Stars Initiative 2019-2020 Scheme.

References

- [1] T. G. Karayiannis and M. M. Mahmoud, "Flow boiling in microchannels: Fundamentals and applications," *Appl. Therm. Eng.*, vol. 115, pp. 1372–1397, Mar. 2017, doi: 10.1016/J.APPLTHERMALENG.2016.08.063.
- [2] K. P. Drummond et al., "A hierarchical manifold microchannel heat sink array for high-heat-flux two-phase cooling of electronics," *Int. J. Heat Mass Transf.*, vol. 117, pp. 319–330, Feb. 2018, doi: 10.1016/J.IJHEATMASSTRANSFER.2017.10.015.
- [3] T. G. Karayiannis and M. M. Mahmoud, "FLOW BOILING IN MICRO-PASSAGES: DEVELOPMENTS IN FUNDAMENTAL ASPECTS AND APPLICATIONS," in 16th International Heat Transfer Conference, IHTC-16, 2018, pp. 203–227.
- [4] T. Harirchian and S. V. Garimella, "Effects of channel dimension, heat flux, and mass flux on flow boiling regimes in microchannels," *Int. J. Multiph. Flow*, vol. 35, no. 4, pp. 349–362, 2009, doi: <https://doi.org/10.1016/j.ijmultiphaseflow.2009.01.003>.
- [5] T. Harirchian and S. V. Garimella, "The critical role of channel cross-sectional area in microchannel flow boiling heat transfer," *Int. J. Multiph. Flow*, vol. 35, no. 10, pp. 904–913, 2009, doi: <https://doi.org/10.1016/j.ijmultiphaseflow.2009.06.005>.
- [6] S. G. Singh, A. Kulkarni, S. P. Duttagupta, B. P. Puranik, and A. Agrawal, "Impact of aspect ratio on flow boiling of water in rectangular microchannels," *Exp. Therm. Fluid Sci.*, vol. 33, no. 1, pp. 153–160, Oct. 2008, doi: 10.1016/J.EXPTHERMFLUSCI.2008.07.014.
- [7] B. Markal, O. Aydin, and M. Avci, "Effect of aspect ratio on saturated flow boiling in microchannels," *Int. J. Heat Mass Transf.*, vol. 93, pp. 130–143, Feb. 2016, doi: 10.1016/J.IJHEATMASSTRANSFER.2015.10.024.
- [8] B. Markal, O. Aydin, and M. Avci, "Prediction of Heat Transfer Coefficient in Saturated Flow Boiling Heat Transfer in Parallel Rectangular Microchannel Heat Sinks: An Experimental Study," *Heat Transf. Eng.*, vol. 38, no. 16, pp. 1415–1428, Nov. 2017, doi: 10.1080/01457632.2016.1255038.
- [9] Y. Wang, K. Sefiane, and S. Harmand, "Flow boiling in high-aspect ratio mini- and micro-channels with FC-72 and ethanol: Experimental results and heat transfer correlation assessments," *Exp. Therm. Fluid Sci.*, vol. 36, pp. 93–106, 2012, doi: <https://doi.org/10.1016/j.expthermflusci.2011.09.001>.
- [10] U. Soupremanien, S. Le Person, M. Favre-Marinet, and Y. Bultel, "Influence of the aspect ratio on boiling flows in rectangular mini-channels," *Exp. Therm. Fluid Sci.*, vol. 35, no. 5, pp. 797–809, Jul. 2011, doi: 10.1016/J.EXPTHERMFLUSCI.2010.06.014.
- [11] P.-S. Lee and S. V. Garimella, "Thermally developing flow and heat transfer in rectangular microchannels of different aspect ratios," *Int. J. Heat Mass Transf.*, vol. 49, no. 17–18, pp. 3060–3067, Aug. 2006, doi: 10.1016/J.IJHEATMASSTRANSFER.2006.02.011.
- [12] P.-S. Lee and S. V. Garimella, "Saturated flow boiling heat transfer and pressure drop in silicon microchannel arrays," *Int. J. Heat Mass Transf.*, vol. 51, no. 3, pp. 789–806, 2008, doi: <https://doi.org/10.1016/j.ijheatmasstransfer.2007.04.019>.
- [13] Y. Wang and K. Sefiane, "Effects of heat flux, vapour quality, channel hydraulic diameter on flow

- boiling heat transfer in variable aspect ratio micro-channels using transparent heating,” *Int. J. Heat Mass Transf.*, vol. 55, no. 9, pp. 2235–2243, 2012, doi: <https://doi.org/10.1016/j.ijheatmasstransfer.2012.01.044>.
- [14] B.-R. Fu, C.-Y. Lee, and C. Pan, “The effect of aspect ratio on flow boiling heat transfer of HFE-7100 in a microchannel heat sink,” *Int. J. Heat Mass Transf.*, vol. 58, no. 1–2, pp. 53–61, Mar. 2013, doi: 10.1016/J.IJHEATMASSTRANSFER.2012.11.050.
- [15] A. Candan, B. Markal, O. Aydin, and M. Avci, “Saturated flow boiling characteristics in single rectangular minichannels: effect of aspect ratio,” *Exp. Heat Transf.*, vol. 31, no. 6, pp. 531–551, Nov. 2018, doi: 10.1080/08916152.2018.1463305.
- [16] A. H. Al-Zaidi, M. M. Mahmoud, and T. G. Karayiannis, “Flow boiling of HFE-7100 in multi-microchannels: aspect ratio effect,” presented at the 6th Micro and Nano Flows Conf., Atlanta, USA, Sep. 9, 2018.,” 2018.
- [17] J. Lee and I. Mudawar, “Fluid flow and heat transfer characteristics of low temperature two-phase micro-channel heat sinks – Part 1: Experimental methods and flow visualization results,” *Int. J. Heat Mass Transf.*, vol. 51, no. 17, pp. 4315–4326, 2008, doi: <https://doi.org/10.1016/j.ijheatmasstransfer.2008.02.012>.
- [18] J. Lee and I. Mudawar, “Fluid flow and heat transfer characteristics of low temperature two-phase micro-channel heat sinks – Part 2. Subcooled boiling pressure drop and heat transfer,” *Int. J. Heat Mass Transf.*, vol. 51, no. 17, pp. 4327–4341, 2008, doi: <https://doi.org/10.1016/j.ijheatmasstransfer.2008.02.013>.
- [19] M. R. Özdemir, M. M. Mahmoud, and T. G. Karayiannis, “Flow boiling heat transfer in a rectangular copper microchannel,” 2015.
- [20] H. Wang, Z. Chen, and J. Gao, “Influence of geometric parameters on flow and heat transfer performance of micro-channel heat sinks,” *Appl. Therm. Eng.*, vol. 107, pp. 870–879, 2016, doi: <https://doi.org/10.1016/j.applthermaleng.2016.07.039>.
- [21] D. R. S. Raghuraman, R. Thundil Karuppa Raj, P. K. Nagarajan, and B. V. A. Rao, “Influence of aspect ratio on the thermal performance of rectangular shaped micro channel heat sink using CFD code,” *Alexandria Eng. J.*, vol. 56, no. 1, pp. 43–54, 2017, doi: <https://doi.org/10.1016/j.aej.2016.08.033>.
- [22] M. Magnini and O. K. Matar, “Numerical study of the impact of the channel shape on microchannel boiling heat transfer,” *Int. J. Heat Mass Transf.*, vol. 150, p. 119322, 2020, doi: <https://doi.org/10.1016/j.ijheatmasstransfer.2020.119322>.
- [23] A. Georgoulas, P. Koukouvini, M. Gavaises, and M. Marengo, “Numerical investigation of quasi-static bubble growth and detachment from submerged orifices in isothermal liquid pools: The effect of varying fluid properties and gravity levels,” *Int. J. Multiph. Flow*, vol. 74, pp. 59–78, 2015, doi: 10.1016/j.ijmultiphaseflow.2015.04.008.
- [24] A. Georgoulas, M. Andredaki, and M. Marengo, “An enhanced VOF method coupled with heat transfer and phase change to characterise bubble detachment in saturated pool boiling,” *Energies*, vol. 10, no. 3, 2017, doi: 10.3390/en10030272.
- [25] E. Teodori, P. Pontes, A. Moita, A. Georgoulas, M. Marengo, and A. Moreira, “Sensible heat transfer during droplet cooling: Experimental and numerical analysis,” *Energies*, vol. 10, no. 6, 2017, doi: 10.3390/en10060790.
- [26] P. Pontes, R. Cautela, E. Teodori, A. S. Moita, A. Georgoulas, and A. L. N. M. Moreira, “Bubble Dynamics and Heat Transfer on Biphilic Surfaces: Experiments and Numerical Simulation,” *J. Bionic Eng.*, 2020, doi: 10.1007/s42235-020-0064-x.
- [27] M. Andredaki, A. Georgoulas, N. Miché, and M. Marengo, “Accelerating Taylor bubbles within circular capillary channels: Break-up mechanisms and regimes,” *Int. J. Multiph. Flow*, vol. 134, 2021, doi: 10.1016/j.ijmultiphaseflow.2020.103488.
- [28] K. Vontas, M. Andredaki, A. Georgoulas, N. Miché, and M. Marengo, “The effect of surface wettability on flow boiling characteristics within microchannels,” *Int. J. Heat Mass Transf.*, vol. 172, p. 121133, 2021, doi: <https://doi.org/10.1016/j.ijheatmasstransfer.2021.121133>.
- [29] K. Vontas, M. Andredaki, A. Georgoulas, K. S. Nikas, and M. Marengo, “Numerical Investigation of Droplet Impact on Smooth Surfaces with Different Wettability Characteristics: Implementation of a dynamic contact angle treatment in OpenFOAM,” in *28th European Conference on Liquid Atomization and Spray Systems*, 2017, doi: <http://dx.doi.org/10.4995/ILASS2017.2017.5020>.
- [30] J. . Brackbill, D. . Kothe, and C. Zemach, “A continuum method for modeling surface tension,” *J.*

- Comput. Phys., vol. 100, no. 2, pp. 335–354, Jun. 1992, doi: 10.1016/0021-9991(92)90240-Y.
- [31] S. Hardt and F. Wondra, “Evaporation model for interfacial flows based on a continuum-field representation of the source terms,” *J. Comput. Phys.*, vol. 227, no. 11, pp. 5871–5895, 2008, doi: 10.1016/j.jcp.2008.02.020.
- [32] A. Georgoulas, M. Andredaki, and M. Marengo, “An Enhanced VOF Method Coupled with Heat Transfer and Phase Change to Characterise Bubble Detachment in Saturated Pool Boiling,” *Energies*, vol. 10, no. 3, p. 272, Feb. 2017, doi: 10.3390/en10030272.
- [33] S. F. Kistler, “In Hydrodynamics of Wetting,” in *Wettability*, no. 1993, J. C. Berg, Ed. (Dekker, New York, 1993), 1993, pp. 311-429.
- [34] P. Pontes, R. Cautela, E. Teodori, A. Moita, A. Georgoulas, and A. L. N. Moreira, “Bubble dynamics and heat transfer on biphilic surfaces,” in *Proceedings of the 16th UK Heat Transfer Conference (UKHTC2019)*, 2019, p. 3.
- [35] A. Mukherjee, S. G. Kandlikar, and Z. J. Edel, “Numerical study of bubble growth and wall heat transfer during flow boiling in a microchannel,” *Int. J. Heat Mass Transf.*, vol. 54, no. 15, pp. 3702–3718, 2011, doi: <https://doi.org/10.1016/j.ijheatmasstransfer.2011.01.030>.
- [36] K. Ling, G. Son, D.-L. Sun, and W.-Q. Tao, “Three dimensional numerical simulation on bubble growth and merger in microchannel boiling flow,” *Int. J. Therm. Sci.*, vol. 98, pp. 135–147, 2015, doi: <https://doi.org/10.1016/j.ijthermalsci.2015.06.019>.
- [37] L. E.W., I. H. Bell, M. L. Huber, and M. O. McLinden, “REFPROP Documentation Release 10.0.” 2018.